Lithologic controls on microfracturing from legacy underground nuclear explosions

Swanson, Erika M
Wilson, Jennifer E.
Sussman, Aviva J.

To be published in: GSA Bulletin

DOI to publisher's version: 10.1130/B36466.1

THE GEOLOGICAL SOCIETY OF AMERICA®

Lithologic controls on microfracturing from legacy underground nuclear explosions

Erika M. Swanson[1,†], Jennifer E. Wilson[2], and Aviva J. Sussman[3]

[1]*Los Alamos National Laboratory, EES-14, P.O. Box 1663 MS D452, Los Alamos, New Mexico 87545, USA*

[2]*Sandia National Laboratories, Geomechanics Department, P.O. Box 5800 MS 0735, Albuquerque, New Mexico 87185-0735, USA*

[3]*Sandia National Laboratories, Nuclear Verification Department, P.O. Box 5800 MS 1373, Albuquerque, New Mexico 87185-1373, USA*

ABSTRACT

Detection and verification of underground nuclear explosions (UNEs) can be improved with a better understanding of the nature and extent of explosion-induced damage in rock and the effect of this damage on radionuclide migration. Much of the previous work in this area has focused on centimeter- to meter-scale manifestations of damage, but to predict the effect of damage on permeability for radionuclide migration, observations at smaller scales are needed to determine deformation mechanisms. Based on studies of tectonic deformation in tuff, we expected that the heterogeneous tuff layers would manifest explosion-induced damage differently, with welded tuffs showing more fractures and nonwelded tuffs showing more deformation bands. In comparing post-UNE samples with lithologically matched pre-UNE equivalents, we observed damage in multiple lithologies of tuff through quantitative microfracture densities. We find that the texture (e.g., from deposition, welding, alteration, etc.) affects fracture densities, with stronger units fracturing more than weaker units. While we see no evidence of expected deformation bands in the nonwelded tuffs, we do observe, as expected, much larger microfracture densities at close range (<50 m) to the explosive source. We also observe a subtle increase in microfracture densities in post-UNE samples, relative to pre-UNE equivalents, in all lithologies and depths. The fractures that are interpreted to be UNE-induced are primarily transgranular and grain-boundary microfractures, with intragranular microfracture densities being largely similar to those of pre-UNE samples. This work has implications for models of explosion-induced damage and how that damage may affect flow pathways in the subsurface.

INTRODUCTION

The ability to detect and verify an underground nuclear test is of great importance for national and global security. One way of monitoring for nuclear tests is through the detection of radionuclides, which are produced by the nuclear explosion and may reach the atmosphere after migration through pathways in the rocks (e.g., Carrigan and Sun, 2014). These pathways include those fractures formed via both natural (primarily thermal and tectonic) processes and explosion-induced damage. To improve the ability to identify, locate, and characterize underground nuclear explosions (UNEs), a better understanding of the behavior of the rock response to natural and explosion-induced damage, and how that response manifests as observables, is required (Jordan et al., 2015). To this end, a multidisciplinary, multiorganizational project called the Underground Nuclear Explosion Signatures Experiment (UNESE) was conducted and involved the collection and analysis of rock samples from coreholes in the vicinity of two legacy UNEs.

A key "smoking gun" for detecting underground nuclear explosions is the detection of certain radionuclide gases (Carrigan and Sun, 2014), which can break through to the surface days to months after the explosion. Predicting the timing of radionuclide release is important, but it is challenging to model and heavily dependent on the predicted damage (Jordan et al., 2015).

Two aspects of the damage zone are important for the detection and verification of UNEs: the extent and the effect on permeability. Regarding the extent of the damage zone, there is little consistency in how this is modeled in radionuclide gas migration studies. Some radionuclide gas migration studies do not include explicit damage zones at all (e.g., Carrigan et al., 1996; Lowrey et al., 2013); other such studies either use limited, simplified spherical damage zones or narrow cylindrical collapse zones (Sun and Carrigan, 2014; Bourret et al., 2019; Carrigan et al., 2020). Collectively, these studies show that a lack of understanding of the lithologic control on UNE-induced damage is hindering the ability to more realistically model radionuclide gas migration from nuclear tests.

The Nevada National Security Site (NNSS; formerly the Nevada Test Site) is the host to an extensive suite of legacy underground nuclear explosions (U.S. Department of Energy, 2015), many of which occurred in volcanic tuffs. Previous work has identified damage within tuffs in relation to expected, simplified damage zones (Wilmarth, 1959; Carroll and Lacomb, 1993; Martin et al., 1993; Pawloski, 1999; Prothro and Warren, 2001), but they lack a systematic analysis of how damage may vary due to heterogeneities within the tuff layers. Identifying damage in a volcanic tuff sequence is particularly difficult because the subsurface layers are heterogeneous, with an enormous range of physical and mechanical properties (strength, porosity, seismic velocity, etc.; e.g., Martin et al., 1993; Moon, 1993; Riley et al., 2010; Broome et al., 2019). This leads to significant challenges in identifying UNE-induced damage, which can produce changes in physical and material properties that are still within the wide range of those of undamaged samples. Here, we attempt to identify the full extent of damage, including more subtle damage, by subdividing the subsurface samples into classes of lithologies within which the material properties have less variation than the overall tuff. We analyzed the material properties of both undamaged (pre-UNE) and damaged (post-UNE) samples, separated them into similar textures, and observed changes indicative of more extensive, subtle damage.

The second important aspect of damage is the effect on permeability (e.g., Jordan et al., 2015).

Erika M. Swanson https://orcid.org/0000-0002-2238-010X

[†]emswanson@lanl.gov.

GSA Bulletin;
published online 21 October 2022

https://doi.org/10.1130/B36466.1; 6 figures; 3 tables; 1 supplemental file.

The next step is understanding, at a small scale, how damage is expressed in rocks: if large, transgranular fractures are opening, this provides fast pathways for radionuclides. In contrast, if damage is contained within individual grains, there is no continuous path for gases, and permeability may not be enhanced at all. A first attempt to relate damage to permeability was done by Jordan et al. (2015), but this is based on a qualitative damage assessment in granite and does not apply to porous material like tuff or to any material with variable properties. Thus, a better quantitative relationship between damage and permeability is needed for different lithologies of tuff. Here we present data on how different tuff lithologies manifest damage differently in terms of the microstructure.

Quantitative microfracture analyses of explosion-induced damage in a tuff sequence with varying lithologies, have, to our knowledge, never been done before. The closest analysis was a study by Borg (1970), which showed a relationship between qualitative UNE-induced fracture intensity and mechanical properties in a stratigraphy of sandstones and shales, with the stronger sandstones showing more fracturing. However, it is unclear how to translate these results to a volcanic sequence, and the qualitative description of the fractures may have missed subtle, more distal damage. By not considering lithologic controls on fracturing, previous work may have missed more subtle damage in the many UNEs that occurred in tuffs. In addition, by not considering differences in how damage manifests in different tuff layers (e.g., dilatant fractures vs. compactive cataclasis and transgranular vs. intragranular fractures), assumptions about the resulting change in permeability from damage would likely be incorrect.

Here, we present quantitative data on microfractures on damaged and undamaged samples that are segregated into lithologic groups. We discuss how lithology and distance affect the manifestation of UNE-induced damage and the implications for nuclear explosion detection.

GEOLOGIC SETTING

Our study was conducted at two areas near legacy UNEs: one near Barnwell and one near Disko Elm (Fig. 1). Both sites lie within the Miocene Southwest Nevada Volcanic Field, which includes silicic ash-flow tuffs, bedded tuffs, and rhyolitic lava from the Calico Hills Formation (from the Silent Canyon Caldera, 13–14 Ma), the Paintbrush Group (from the Claim Canyon Caldera, 12.7–12.8 Ma), and the Timber Mountain Group (from the Timber Mountain Caldera, 11.5–12.5 Ma; Sawyer et al., 1994). These volcanic rocks have experienced minimal syn-depositional and post-depositional extension, expressed as NNE-striking faults and slight (<5°) tilting of fault blocks (Gibbons et al., 1963; Slate et al., 1999). The Barnwell study area lies between the West Greeley and East Greeley faults, with the nearest splay of the West Greeley fault occurring ~300 m from the study area (Burkhard and Wagoner, 1989). The volcanic sequence deposited in the Disko Elm area comprises a simple, layer cake-like sequence with consistent thicknesses, little lateral variation, and no significant faults within 1 km (Gibbons et al., 1963; Prothro et al., 2009). The lack of fault-related deformation within the volcanic strata at each site allows us to characterize the tuff stratigraphy in terms of petrophysical properties and to evaluate the damage that has occurred in the subsurface due to an underground nuclear explosion.

In general, ash-flow tuffs are spatially heterogeneous pyroclastic flow deposits that consist of a poorly sorted assemblage of ash (volcanic glass shards less than 4 mm in size), pumice, phenocrysts, and lithic fragments. These tuffs commonly form individual cooling units, within which there is a range in the degree of welding and post-depositional crystallization. Among individual cooling units, lava flows may be deposited, and these commonly consist of flow banding with varying degrees of crystallization and alteration. The volcanic sequences studied here fit this description well and are described in detail in terms of published stratigraphic nomenclature below.

The Ammonia Tanks member of the Timber Mountain Group, a partially to non-welded, vitric ash-flow tuff and bedded ash- and pumice-fall deposit (Prothro, 2018), crops out at the surface above both UNEs (Fig. 1), but this unit is sampled only at Disko Elm. Below the Ammonia Tanks Tuff is the Rainier Mesa member of the Timber Mountain Group (Fig. 2), a nearly 150-m-thick sequence that includes partially to strongly welded ash-flow tuff that has partial to complete devitrification and vapor-phase crystallization; overlying vitric, nonwelded ash-flow tuff; bedded ash- and pumice-fall deposits; and reworked tuff with variable amounts of alteration of glass to clay-sized minerals. At Barnwell, a vitrophyric ash-flow tuff deposit separates the strongly welded and nonwelded portions of the Rainier Mesa member. This is absent at Disko Elm. The nonwelded tuff at the bottom of the Rainier Mesa member lies above a vitric, nonwelded ash-flow tuff of the Paintbrush Group (Rhyolite of Echo Peak and Tiva Canyon Tuff) at Barnwell and the vitric, nonwelded Tuff of Holmes Road at Disko Elm (Burkhard and Wagoner, 1989; Prothro, 2018). Below these intervals, the Calico Hills Formation continues in each location's coreholes. At Barnwell, the Calico Hills Formation includes the following lithologies with increasing depth: vitric, nonwelded ash-flow tuff; partially zeolitic, nonwelded bedded ash- and pumice-fall deposits; an interval of vitric, rhyolitic lava; and completely zeolitized, nonwelded bedded ash- and pumice-fall deposits (Burkhard and Wagoner, 1989). At Disko Elm, the Calico Hills Formation transitions downward gradually from vitric, nonwelded ash-flow tuff to zeolitic, nonwelded ash-flow and pyroclastic-fall deposits of the Wahmonie Formation and Crater Flat Group (Prothro, 2018).

Figure 1. Maps of sample locations show (A) the location within the Nevada National Security Site (NNSS); caldera geometries are from Prothro and Warren (2001) and faults are from Slate et al., (1999). Also shown are the locations of coreholes used for pre-Barnwell samples. (B) Map shows location of the Barnwell study area and nearby sample locations of post-shot core U20az-NG4, as well as the source hole U20az. (C) Location map for Disko Elm study area shows locations of vertical coreholes and the surface projection of the Disko Elm event location (U12p.03).

METHODS

Core was retrieved from near two legacy UNE sites, Barnwell and Disko Elm, which share a similar ash-flow tuff stratigraphy at the Nevada National Security Site (Fig. 2). We collected core from near U-20az, the site of the 1989 Barnwell test, located on Pahute Mesa within the Nevada National Security Site (Fig. 1). This test was 601 m deep in a vertical shaft in volcanic tuff, with an announced yield between 20 kt and 150 kt of TNT equivalent (U.S. Department of Energy, 2015). We also collected core from the U12p Tunnel, the site of the 1989 Disko Elm test, located at Aqueduct Mesa. This test was ~261 m deep in a tunnel, also in volcanic tuff (Prothro, 2018; Wagner et al., 2018), with an announced yield of less than 20 kt (U.S. Department of Energy, 2015). These explosions both occurred within zeolitic, nonwelded tuffs.

There is currently no way to readily distinguish explosion-induced fractures from natural, pre-existing ones. Previous fracture studies that consider the timing of multiple sets of microfractures commonly find that filled or sealed microfractures reflect pre-existing fractures, while open ones could be either new or pre-existing (Wilson et al., 2003a; Perez and Boles, 2005; Gale and Gomez, 2007; Mitchell and Faulkner, 2009; Anders et al., 2014). This open vs. filled criteria has been used to distinguish

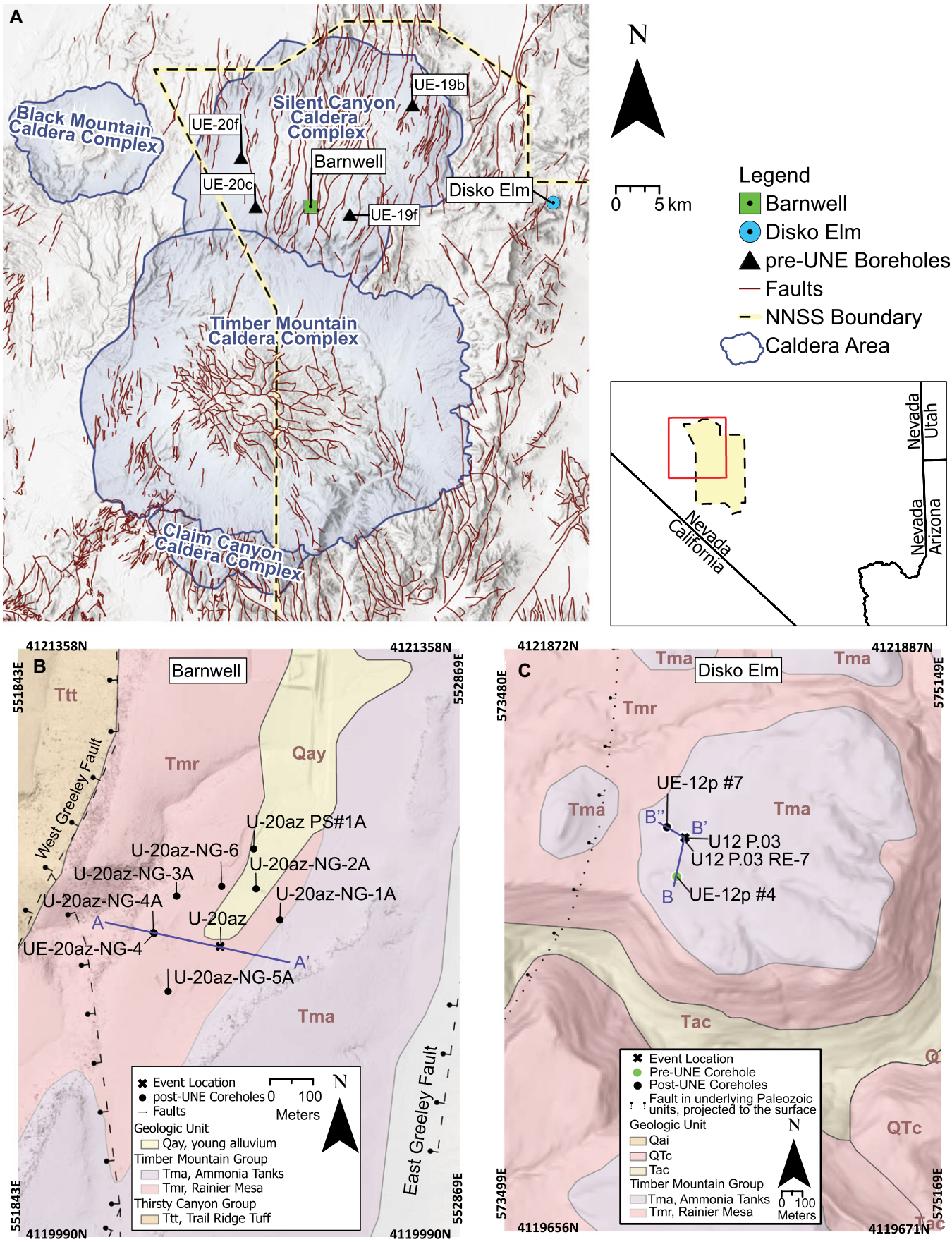

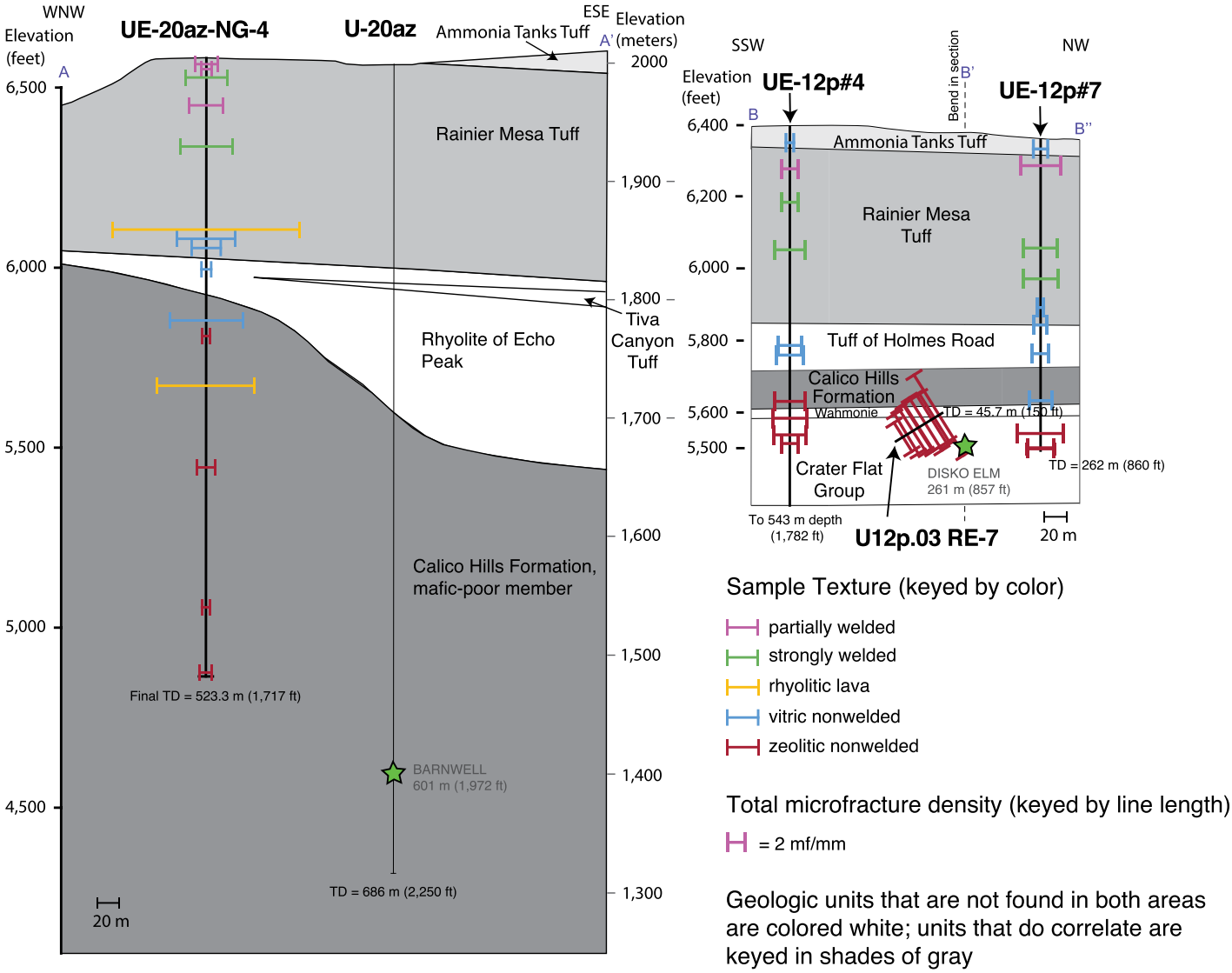

Figure 2. Cross-sections allow for comparison of the geologic units between the Barnwell and Disko Elm sites (left and right, respectively). Cross-section lines are shown in Figure 1 and include a large bend at B′ to preserve distances from the explosion for all samples. Units that are only found in one site are colored white, while units that correlate among sites are keyed in shades of gray. Also shown are microfracture densities, which are keyed by lithology (data in Table 3). The same vertical scale and microfracture density scale are used for both sites. UE-12p#4 was drilled in 1987, prior to all P-tunnel nuclear explosions, including Disko Elm. All other samples shown are from post-underground nuclear explosion cores. TD—total depth.

explosion-induced fractures from pre-existing fractures (e.g., Borg, 1970). However, recent work has shown that explosion-induced fractures may not still be open at the time of sample collection, due to rapid precipitation of clays within fractures (Swanson et al., 2019). Thus, we believe the best way to identify explosion-induced damage is by comparing total numbers of fractures with similar samples that have not undergone explosive shock ("pre-UNE"), aiming to match welding and postdepositional characteristics, as described below.

Pre-UNE samples were collected from core curated at the U.S. Geological Survey Mercury Core Library. These samples came from coreholes that were drilled prior to any underground nuclear tests in the immediate area (within a few kilometers). At Barnwell, pre-UNE samples come from vertical coreholes UE-19b, UE-19f, UE-20c, and UE-20f (Fig. 1A, black triangles); post-UNE samples are from vertical coreholes UE-20az-NG4 and UE-20az-NG6 (Fig. 1B, black circles). At Disko Elm, pre-UNE samples are from vertical corehole UE-12p#4 (Fig. 1C, green circle); post-UNE samples are from vertical corehole UE-12p#7 and tunnel-level angled (upward at 30° from horizontal) corehole U12p.03 RE-7 (Fig. 1C, black circles, but RE-7 is obscured by the UNE location). All of the post-UNE core has the same diameter, and similar drilling techniques were used. Drilling fluids included water and soap/polymer during standard core recovery, with the addition of bentonite mud, ground nut shells, cellophane, etc., in portions where recovery was difficult (caving, stuck tools, etc.). These core intervals, as well as portions of core that were broken mechanically at the rig-site, were avoided for this study. Sample handling and storage may also affect core characteristics, and core that has been sitting in boxes for several months to years may dry out or otherwise change. To minimize the effects

of sample storage for the Disko Elm samples, we preferentially selected cores that had been wrapped in wax and foil, a technique designed to maintain in situ water content.

Recovered core from the majority of each corehole was inspected and categorized into different lithologies, based on our core-scale, qualitative observations of induration, pumice morphology, vitric content, presence of alteration, and alignment of components. Lengths of core characterized totaled 1.6 m from five pre-Barnwell coreholes, 23.8 m from two post-Barnwell coreholes, 8.2 m from one pre-Disko Elm corehole, and 9.8 m from two post-Disko Elm coreholes. Samples for optical microscopy analysis were chosen to encompass the variety of welding and postdepositional crystallization textures, as determined by these core descriptions. Thin-section samples that would serve as pre- and post-UNE analogues were chosen based on similar core-scale characteristics (induration, component characteristics, etc.) and sample handling procedures (dry versus waxed). Thin section billets were prepared using a diamond blade saw or wire saw (friable samples required a wire saw), and tap water was used for cooling. Two standard petrographic thin sections, 27 × 46 mm in dimension and 30 μm in thickness, were made from each sample, with one parallel to the core axis and the other perpendicular.

Petrography, microtextures, and microfractures from Barnwell core thin sections were observed and imaged on an Olympus Polarizing Microscope with CellSens imaging software. Observations and images from Disko Elm thin sections were obtained on a Leitz Wetzlar Orthoplan Microscope with Leica LAS X imaging software, which is available from Leica and is commonly used with Leica microscope systems. Relative amounts of components (pumice, phenocryst, lithic fragment, and matrix ash/glass) were quantified by performing point count analysis on each thin section with a 800–1000 point grid with 1 mm spacing. The degree of welding for each sample was quantified by measuring the aspect ratio (pumice width divided by height) of at least 10 pumice clasts per thin section.

Microfractures were identified as open or filled, transgranular, intragranular, or grain boundary, and their quantities were recorded as a linear density using a 20× (Barnwell) or 16× (Disko Elm) objective. All microfractures that cross the horizontal crosshair when viewed at these magnifications were recorded at 50 locations per thin section, two thin sections per sample, with the orientation of the thin section randomized by spinning the microscope stage (e.g., Wilson et al., 2003a). This randomization of the orientation of the counting line ensures an un-biased measure of 3-D objects that are being measured on a 2-D surface (e.g., Underwood, 1970). Linear microfracture density was calculated for each microfracture type as number of microfractures per millimeter.

Scanning electron microscopy of selected samples was performed using a TESCAN Vega3 scanning electron microscope (SEM). The thin sections were first coated with a gold-palladium alloy using a Denton Vacuum Desk IV sputter-coater. Microtexture of each thin section was observed and imaged using backscattered electrons (BSE) and secondary electrons (SE) in high-vacuum mode at an accelerating voltage of 20.0 kV. Microporosity was quantified for each sample by calculating the percentage of black pixels in at least five BSE images (1 mm × 1 mm area) at 1 μm resolution for each sample. Images were processed using segmentation methods that identify each pixel in the image as either porosity or tuff material. This was done manually for all images using the threshold tool, which divides the image into two classes of pixels (black for porosity, gray for tuff material), and visual matching of pore space with the original BSE image in ImageJ (e.g., Lange et al., 1994). To confirm presence of glass versus devitrification or alteration minerals, elemental compositions from unaltered and altered portions of most thin sections were obtained using an EDAX energy-dispersive (EDS) system at an accelerating voltage of 15.0 kV. EDS spectra were collected and analyzed using the TEAM EDS analysis system for the SEM.

RESULTS

Lithologic Categorization and Characterization

To examine the role of differing lithologies on microfracture characteristics, we divided samples into five lithologic categories (Fig. 3). Listed from top to bottom at the Barnwell site, the five categories are: partially welded (PW) ash-flow tuff; strongly welded (SW) ash-flow tuff; rhyolitic lava (RL); vitric, nonwelded (VN) ash-flow tuff; and zeolitic, nonwelded (ZN) ash-flow tuff. Four of the lithologic categories found at Barnwell also exist at Disko Elm; the rhyolitic lava (RL) is absent from Disko Elm cores. This categorization largely aligns with hydrologic framework model layers defined at Disko Elm (Prothro, 2018) and has been used in a parallel effort to document multiphase flow properties of these lithologies (Heath et al., 2021).

Categorization is based on welding, postdepositional crystallization, and vitric content. Welding is the flattening and/or fusion of ash and pumice during compaction under sufficiently high eruption temperature (>650 °C), load induced by overlying deposits, and plays a primary role in controlling the textures studied in this investigation. The process of welding usually occurs within days of initial deposition (Ross and Smith, 1961), during which time volcanic glass is sufficiently hot to plastically compact around more competent phenocrysts and lithic fragments. The degree of welding can be quantified by bulk density, porosity, or pumice aspect ratio measurements. Since some samples in our study are affected by postdepositional alteration (i.e., glass to smectite and/or zeolite) and may be affected by explosion-induced deformation, and thus may have damage-related porosity variations, we used pumice aspect ratio measured in thin section to categorize units: 1.4–2.4 = nonwelded, 2.2–4.4 = partially welded, and 4.1–17.5 = strongly welded. Where there is minor overlap in these pumice aspect ratios, induration at grain contacts (via microscale observations and core sample induration tests) is used to further categorize a particular sample.

Postdepositional crystallization in this study occurs as (1) devitrification and vapor-phase crystallization to alkali feldspar/quartz polymorph crystal aggregates in PW and SW units, (2) as fluid-assisted alteration to zeolite in ZN units, and (3) as alteration of glass to smectite in VN and ZN units. These characteristics are described qualitatively and confirmed by EDS analyses of minerals in thin section.

Partially Welded

PW ash-flow tuff is composed of phenocrysts, pumice, and lithic fragments in a matrix of slightly to moderately compacted glass shards, pumice fragments, and ash (Fig. 3A). Pumice is also partially flattened, with aspect ratios ranging from 2.2 to 4.4 (Tables 1 and 2), which imparts a slight to moderate anisotropy to this type of unit. This compaction indurates the rock so that it holds together during routine handling but is easily scratched with a nail. EDS analyses indicate that the partially welded ash-flow tuff in this study contains no glass; devitrification and vapor-phase crystallization have converted volcanic glass to alkali feldspar and silica polymorphs, cristobalite, and tridymite. Microporosities range from 12.4% to 29.2%, with most variations due to varying degrees of vapor-phase crystallization of dissolved glass, which left some isolated, remnant pumice voids. This unit is sampled in two different pre-Barnwell cores and is present in the post-Barnwell core (UE-20az-NG-4 and UE-20az-NG-6) at drilling depths of 7.3–65.5 m with a strongly welded interval at 18.9–22.6 m drilling depth (Fig. 2). At Disko Elm, PW is overlain by VN and is found as a much thinner unit at drilling depths of 21.9–44.2 m in the pre-Disko Elm core

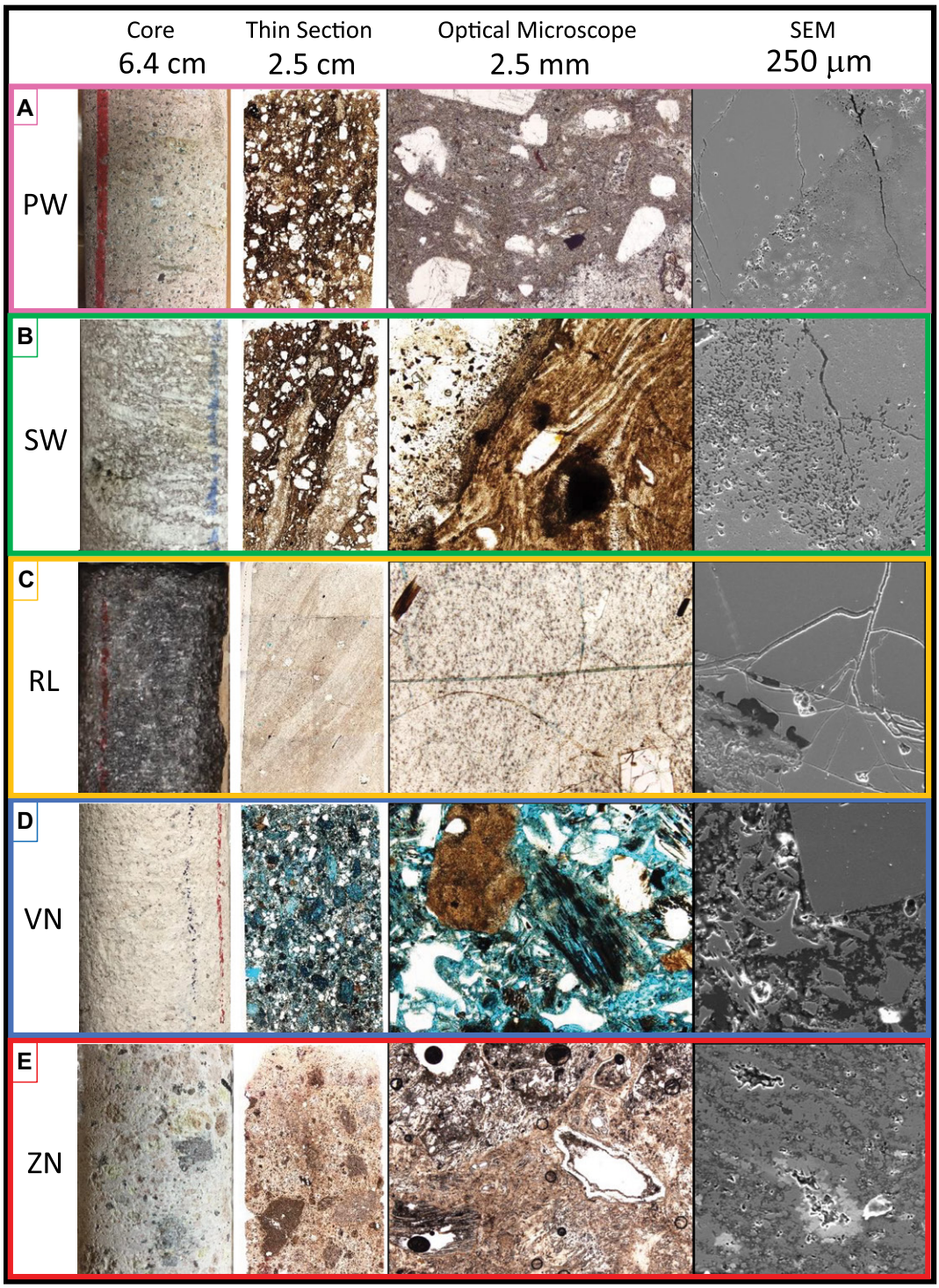

Figure 3. Examples of the lithologic textural categories used here are shown: (A) partially welded ash-flow tuff (PW); (B) strongly welded ash-flow tuff (SW); (C) rhyolitic lava and vitrophyre (RL); (D) vitric, nonwelded ash-flow tuff (VN); and (E) zeolitized nonwelded ash-flow tuff (ZN). Shown are core photos (width of image = 6.4 cm), thin section scans at the centimeter scale (width of image = 2.5 cm), optical microscope images at the millimeter scale (width of image = 250 µm), and scanning electron microscopy images at the micron scale. Core, thin section, and optical microscope images are from post-underground nuclear explosion (UNE) samples; micron-scale images are secondary electron (SE) images from pre-UNE samples.

(UE-12p#4) and 15.2–29.9 m in the post-Disko Elm core (UE-12p#7).

Strongly Welded

SW ash-flow tuff is composed of phenocrysts, pumice, and lithic fragments surrounded by a highly compacted matrix of crystallized volcanic ash, glass shards, and pumice fragments (Fig. 3B). Flattened pumice (fiamme, with aspect ratios ranging from 4.1 to 17.5) commonly defines a strong anisotropy in this unit (Tables 1 and 2). Welding and postdepositional crystallization make this rock completely indurated with very limited pore space (microporosities range from 6.7% to 9.9%). This unit is sampled in three pre-Barnwell cores and is found as a thin layer from 18.9 m to 22.6 m within the PW unit, as well as from 65.8 m to 143.0 m drilling depths in post-Barnwell core (UE-20az-NG-4; Fig. 2). The SW unit is present from 44.2 m to 146.3 m in pre-Disko Elm core (UE-12p#4) and 29.9–127.1 m in post-Disko Elm core (UE-12p#7). Variations in textures within this unit include a large range in pumice aspect ratio (very high aspect ratios in

TABLE 1. COMPARISON OF AVERAGE COMPOSITIONS, MICROPOROSITIES, AND MICROFRACTURE DENSITIES BETWEEN PRE-BARNWELL AND POST-BARNWELL LITHOLOGIES

Ash-flow tuff	Groundmass	Phenocrysts	Pumice	Lithics	Pumice AR	Microporosity	Microfracture densities (mf/mm)
Average pre-PW	64	11	20	5	3.1	13.9	1.0
Average post-PW	55	21	20	4	3.5	21.5	2.5
Average pre-SW	59	22	15	4	4.5	12.9	3.4
Average post-SW	43	38	14	5	13.7	9.7	4.8
Pre-VN	74	14	9	4	1.5	49	1.8
Average post-VN	54	15	27	5	1.5	39.2	4.4
Average pre-RL	69	13	17	1	2	6	3.4
Average post-RL	83	11	6	0	6.5	2	14.2
Pre-ZN	41	11	43	6	1.8	36.2	1.3
Average post-ZN	47	3	34	16	1.9	14.5	1.4

Notes: These data show greater variability within each lithology relative to Disko Elm samples. All values are in % except for microfracture densities (microfractures/millimeter [mf/mm]) and pumice aspect ratio (AR = pumice length divided by height). Microporosity is calculated separately from percentages of tuff components (see description in Methods section), which may cause total percentages to be >100%. PW—partially welded; SW—strongly welded; VN—nonwelded; RL—rhyolitic lava; ZN—nonwelded.

TABLE 2. COMPARISON OF AVERAGE COMPOSITIONS, MICROPOROSITIES, AND MICROFRACTURE DENSITIES BETWEEN PRE-DISKO ELM AND POST-DISKO ELM LITHOLOGIES

Ash-flow tuff	Groundmass	Phenocrysts	Pumice	Lithics	Pumice AR	Microporosity	Microfracture densities (mf/mm)
Pre-VN shallow	59	26	13	2	2.4	55.4	1.0
Post-VN shallow	58	14	22	6	2.2	42.6	1.7
Pre-PW	60	19	19	2	3.3	25.6	2.0
Post-PW	59	16	20	5	3.4	29.2	4.2
Average pre-SW	49	16	22	13	6.5	7.2	2.6
Average post-SW	56	16	24	4	6.1	5.1	3.6
Average pre-VN deep	31	15	43	11	1.6	31.2	2.8
Average post-VN deep	37	11	45	7	1.8	28.2	1.7
Average pre-ZN	48	15	33	4	1.7	22	3.1
Average post-ZN	46	16	34	4	1.7	17.4	3.3

Notes: All columns are in %, except for microfracture densities (microfractures/millimeter [mf/mm]) and pumice aspect ratio (AR = pumice length divided by height). Microporosity is calculated separately from percentages of tuff components (see descriptions in Methods section), which may cause total percentages to be >100%. PW—partially welded; SW—strongly welded; VN—nonwelded; RL—rhyolitic lava; ZN—nonwelded.

post-Barnwell core at 73.2 m) and in the degree of devitrification (lack of devitrification in the presence of welding in post-Disko Elm core at 121.9 m). These variations possibly reflect variations in caldera activity (e.g., Gimeno et al., 2003; Repstock et al., 2019) but do not affect the observed induration of the rock.

Rhyolitic Lava and Vitrophyre

RL and vitrophyre is composed of Si-rich volcanic glass (the same composition as glass in all other Barnwell and Disko Elm samples), where the majority or all of the matrix of the unit is vitric (i.e., no devitrification of the volcanic glass) and mechanically homogeneous (Fig. 3C). It is distinct from VN ash-flow tuff in that there are no individual glass shards separated by pore space, and the majority of the rock is composed of volcanic glass (i.e., few phenocrysts, pumice, and lithic fragments; Table 1). Microporosities range from 2.9% to 8.6%, and where pumice is present, aspect ratios range from 2.0 to 6.5. RL is found only at the Barnwell site, at drilling depths of 266.7–295.7 m in post-Barnwell core (UE-20az-NG-4; Fig. 2). Vitrophyre samples found at the top of the VN unit at Barnwell (143.0–148.4 m drilling depth in UE-20az-NG-4) are included in the RL category because of their similar characteristics at the core and microscale (few components in highly vitric matrix, low porosity, and conchoidal fracture habit). The two RL samples in pre-Barnwell core are more similar to this vitrophyre than the thicker, deeper RL.

Vitric, Non-Welded

VN ash-flow tuff is composed of phenocrysts, pumice, and lithic fragments in a matrix of volcanic ash, glass shards, and pumice fragments (Fig. 3D). Most glass is still vitric, and there is a large amount of inherent microporosity (29.1%–55.4%; Tables 1 and 2) due to little or no compaction or postdepositional crystallization. Pumice is fairly equant, with pumice ratios ranging from 1.4 to 2.4 and little to no alignment. The VN unit was sampled in one pre-Barnwell core and is present from 143 m to 267 m drilling depths in post-Barnwell core (UE-20-az; Fig. 2), with a thin vitrophyre unit present from 143.0 m to 148.4 m. Samples are highly variable with respect to grain size distributions (ash content) and the degree of induration at grain contacts. For example, the sample at 176.5 m is very ash-rich, at 220.1 m the sample is more grain-supported than all others, and at 232.9 m the sample is incipiently cemented by zeolite minerals. The VN is more uniform at Disko Elm and is present from 146.3 m to a gradational contact with the ZN unit at 232.3–250.9 m in pre-Disko Elm core (UE-12p#4) and from 127.1 m to 234.7 m in post-Disko Elm core (UE-12p#7; Fig. 2). VN samples at Disko Elm have decreasing ash content, becoming more grain supported, with depth, but all show incipient alteration of volcanic glass and lithic fragments to smectite, and some pores are partially filled with smectite.

Zeolitic Non-Welded

ZN ash-flow tuff is composed of pumice, phenocrysts, and lithic fragments in a matrix of shards and ash that has been partially or completely crystallized into zeolitic minerals (Fig. 3E). The most common zeolite mineral in this unit, as identified by crystal morphology and EDS analyses, is clinoptilolite, with some minor mordenite, which is consistent with zeolite diagenesis in the area (Moncure et al., 1981). These zeolites partially fill original pore spaces, creating an interlocking crystal structure where there were previously individual glass fragments with minimal grain contact. The degree of zeolitization among samples is highly variable, resulting in microporosities ranging from 19.1% to 41.1% (Tables 1 and 2). Isolated voids are relatively common within the matrix and within remnant pumice voids in which zeolite has not completely replaced glass. Opal is also deposited along some of these remnant pumice voids. Pumice content is highest in the ZN compared to all other units, and pumice clasts have aspect ratios ranging from 1.4 to 2.2, which indicates minimal anisotropy in this unit. ZN is sampled in one pre-Barnwell core and is found in post-Barnwell core (UE-20az-NG-4) at 232.9 m as well as from 296.3 m to 516.0 m drilling depths (Fig. 2), with a distinct boundary separating the RL unit. At Disko Elm, the boundary between the overlying VN unit and ZN unit is gradational, with glass content inversely proportional to smectite and zeolite content over a depth range of 232.3–250.9 m in pre-Disko Elm core (UE-12p#4) and from 224.9 m to 249.0 m in post-Disko Elm core (UE-12p#7). Deeper ZN samples in these cores, as well as all samples from the post-Disko Elm, tunnel-level core (U12p.03 RE-7), contain no glass but also have significant smectite content, which is likely a result of alteration from glass before it was zeolitized (e.g., Chipera et al.,

2008). The sample closest to the working point (34.0 m range distance, 39.9 m drilling depth in post-Disko Elm core U12p.03 RE-7) is much more phenocryst-rich than all of the other ZN samples. This sample is highly deformed and may be a block of Wahmonie that has displaced downward from its originally higher position (Huckins-Gang and Townsend, 2018).

Types of Deformation Features

We observed a variety of deformation features, including microfractures, cataclastic grain-crushing, and pore collapse. The microfractures can be categorized based on their relationships with grain boundaries into intragranular, grain-boundary, and transgranular microfractures. All microfractures in pre-UNE ZN samples at Barnwell are intragranular, whereas post-UNE microfractures consist of intragranular, transgranular, and grain-boundary varieties.

Intragranular microfractures (fractures occurring within a phenocryst, lithic fragment, or pumice) were particularly prominent in PW samples (Figs. 4A–4B), SW samples (Fig. 4D), and VN samples (Figs. 4J–4L). It is the only type of microfracture found in pre-UNE ZN units. This type of fracture can be produced by (1) thermal expansion during tuff deposition and cooling (Ross and Smith, 1961), (2) postdepositional damage such as tectonic processes, or (3) from UNE-induced damage.

Grain-boundary microfractures are observed in SW units (Fig. 4D) and in the deep (>200 m) ZN (Figs. 4M–4O) units. Grain-boundary microfractures may indicate stress unloading, such as occurs during the passage of a shock wave (Ogilvie et al., 2011), or thermal stresses, where internal stresses are induced at the grain scale due to mismatches between grains and matrix (e.g., Espinosa and Zavattieri, 2003; Dwivedi et al., 2006; Fensin et al., 2014).

Transgranular microfractures are more commonly observed in indurated units (PW—Figs. 4B–4C; SW—Figs. 4D–4F; and ZN—Figs. 4M–4N). Transgranular microfractures are not common in VN samples. Where they do exist, they may indicate relatively indurated (for VN) regions, enough to support a throughgoing fracture, rather than greater damage. Transgranular microfractures are observed in the vitric matrix of the RL unit (Figs. 4G–4I), but they are distinct from transgranular microfractures in other units: they are low-aperture, concentric sets of microfractures that are similar in form to those from thermal hydration during deposition (e.g., McPhie et al., 1993; Gimeno et al., 2003). In addition to preexisting transgranular microfractures, this type of microfracture may form during a UNE by propagation of, and potentially coalescence of, intragranular and grain-boundary microfractures across consolidated matrix.

Cataclastic grain-crushing and pore collapse is observed in some VN samples (Figs. 4J–4K), but they occur in isolation rather than in continuous but localized form (i.e., deformation band). Therefore, deformation is best quantified in terms of microporosity. In the VN units, this microstructure could be syn- or post-depositional, depending on the nature of cataclasis (i.e., postdepositional fracturing is indicated by pinned grains that are crushed, but the presence of fragmentary material with no obvious signs of grain crushing may indicate either syn- or postdepositional deformation).

Shear zones containing cataclastic grain-crushing, shear microfractures, and pore collapse are rare. They occur in the more consolidated, phenocryst- and smectite-rich ZN sample that is closest (34.0 m range distance) to the Disko Elm working point (see kinked biotite in Fig. 4M). Their presence in only post-UNE samples, along with their proximity to the UNE source, indicates they are the result of UNE-induced damage.

Microfracture Quantification

We quantified the number of all microfractures, sorting by different types—total, transgranular, intragranular, and grain-boundary (Table 3)—and show their relationships with depth (Fig. 5). Each lithology has different proportions of microfracture types (Fig. 5).

Total Microfractures

For Barnwell samples, total microfracture densities for pre-UNE samples range from 0.3 to 4.4 microfractures/mm (mf/mm). The SW and RL lithologies have microfracture densities at the high end of this range (1.8–4.4 mf/mm), and the PW, VN, and ZN units have microfracture densities at the low end of the range (<2.4 mf/mm). Every lithology has at least one post-UNE sample with a greater microfracture density than the maximum pre-UNE sample from that lithology. The RL shows the greatest apparent increase (it includes a sample with 18.6 mf/mm, which is off the scale shown), with post-UNE samples having up to four times more microfractures than pre-UNE samples. However, as discussed in greater detail below, the pre-UNE sample texture may be a poor analogue, and the difference in fracture density may not necessarily be the result of the explosion.

For samples near Disko Elm, total microfracture densities for pre-UNE samples range from 1.0 to 3.6 mf/mm. VN and PW pre-UNE lithologies have microfracture densities at the lower end of this range (1.0–2.9 mf/mm), and the ZN and the SW lithologies have slightly more microfractures (1.9–3.6 mf/mm). For post-UNE samples, every lithology except VN tuff has at least one post-UNE sample with a greater microfracture density than the maximum pre-UNE sample from that lithology (Fig. 5). The most significant increase in post-UNE microfracture densities (over pre-UNE equivalents) occurs in samples from RE-7 that are within 50-m-range distance from the explosion source.

Transgranular Microfractures

Transgranular microfractures also show a general increase in post-UNE microfracture densities compared to pre-UNE equivalents (Fig. 5, Table 3). For Barnwell samples, transgranular microfracture densities for pre-UNE samples range from 0 mf/mm to 1.5 mf/mm. The SW lithology has the most transgranular microfractures (0.5–1.5 mf/mm), and the RL lithology has an intermediate number of transgranular microfractures (∼0.6 mf/mm), while the PW and both VN and ZN lithologies have far fewer fractures (<0.1 mf/mm). Every lithology has at least one post-UNE sample with a greater transgranular microfracture density than the maximum pre-UNE sample from that lithology. The RL shows the greatest apparent increase (it includes a sample with 16.1 mf/mm, which is off the scale shown), with post-UNE samples having up to 25× more microfractures than pre-UNE samples. However, as discussed in greater detail below, the pre-UNE sample texture may be a poor analogue, and the difference in fracture density may not necessarily be the result of the explosion.

For samples near Disko Elm, transgranular microfracture densities for pre-UNE samples range from 0 mf/mm to 0.8 mf/mm. All pre-UNE lithologies have similar numbers of microfractures (0–0.4 mf/mm), but one sample from the SW lithology has slightly more microfractures (0.8 mf/mm). For post-UNE samples, every lithology except VN tuff has at least one post-UNE sample with a greater microfracture density than the maximum pre-UNE sample from that lithology (Fig. 5). The most significant increase in post-UNE microfracture densities occurs in samples that are within 50-m-range distance from the explosion source (Table 3).

Intragranular Microfractures

Intragranular microfractures in PW samples range from no change to nearly doubling in density from pre- to post-UNE samples at both Barnwell and Disko Elm. This range may be

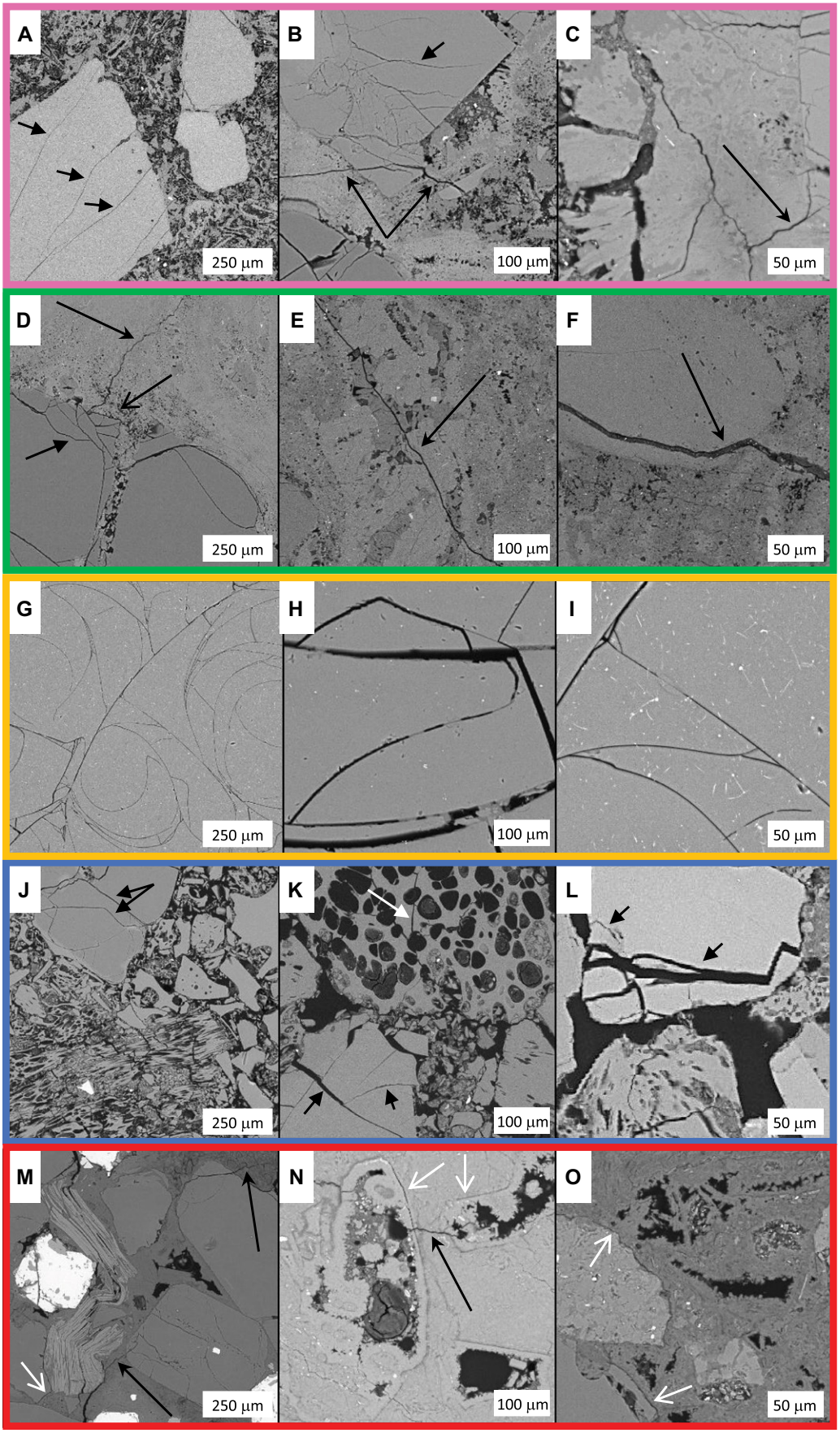

Figure 4. Scanning electron microscopy (backscattered electron) images of microstructures in post-underground nuclear explosion samples from Barnwell and Disko Elm are shown. Partially welded samples in (A), (B), and (C) have variable transgranular microfractures (long stealth arrows) and intragranular microfractures (short block arrows). Strongly welded samples in (D), (E), and (F) also have transgranular and intragranular microfractures. Rhyolitic lava in (G), (H), and (I) are dominated by curvilinear microfractures. Vitric, nonwelded samples (J, K, and L) contain impingement (intragranular) microfractures and nonlocalized pore collapse and grain crushing. Zeolitic, nonwelded samples in (M), (N), and (O) are dominated by grain-boundary (short white arrows) and transgranular microfractures.

TABLE 3. MICROFRACTURE DENSITIES FOR ALL SAMPLES IN THE VICINITY OF BARNWELL AND DISKO ELM WITH RANGE DISTANCES FROM RESPECTIVE UNDERGROUND NUCLEAR EXPLOSION (UNE) SOURCE

Timing relation to UNE	Core name	Lithology of ash-flow tuff	Pumice aspect ratio	Drill depth* (m)	Range distance from UNE source (m)	Transgranular microfracture density (mf/mm)	Grain boundary microfracture density (mf/mm)	Intragranular microfracture density (mf/mm)	Total microfracture density (mf/mm)
Pre-Barnwell	UE-19b	PW	3.7	254	n/a	0.1	0.0	1.6	1.7
	UE-20f	PW	2.5	801	n/a	0	0.0	0.2	0.3
	UE-20c	SW	4.4	199	n/a	1.5	0.0	3.0	4.4
	UE-19b	SW	4.4	154	n/a	1.1	0.0	3.1	4.0
	UE-20c	SW	4.6	648	n/a	0.5	0.0	1.6	1.9
	UE-19b	VN	1.5	106	n/a	0.6	0.0	1.1	1.8
	UE-19f	RL	2	606	n/a	0.4	0.0	4.0	4.4
	UE-19b	RL	2	311	n/a	0	0.0	2.4	2.4
	UE-20c	ZN	1.8	778	n/a	0	0.0	1.3	1.3
Post-Barnwell	UE-20az-NG6	PW	2.8	4	615	0.3	0.4	1.7	2.5
	UE-20az-NG4	PW	3.3	9	614	0.1	0.0	1.3	1.3
		PW	4.4	39	585	0.4	0.0	3.2	3.6
		SW	9.9	20	603	1	0.1	3.3	4.3
		SW	17.5	73	552	1.7	0.2	3.6	5.3
		RL	6.5	143	485	16.1	0.1	2.4	18.6
		VN	2.2	151	477	3.6	0.0	2.0	5.7
		VN	1.7	158	471	0	0.0	3.1	3.1
		VN	1.5	176	454	0.1	0.0	1.1	1.2
		VN	1.6	220	414	0.1	0.0	7.3	7.4
		ZN	1.9	233	402	1	0.1	0.2	1.0
		RL	n/a	274	365	9.7	0.0	0.0	9.8
		ZN	1.9	344	305	0.8	0.4	0.8	2.0
		ZN	1.9	461	217	0.5	0.1	0.6	1.0
		ZN	1.9	516	188	0.7	0.2	0.7	1.5
Pre-DIEL	UE-12p#4	VN	2.4	21	n/a	0	0.0	1.0	1.0
		PW	3.3	43	n/a	0.1	0.0	1.9	2.0
		SW	5.8	71	n/a	0.2	0.0	1.7	1.9
		SW	7.1	111	n/a	0.8	0.1	2.7	3.3
		VN	1.6	191	n/a	0	0.0	2.6	2.6
		VN	1.6	199	n/a	0.2	0.3	2.4	2.9
		ZN	1.5	238	n/a	0.2	0.0	3.1	3.3
		ZN	1.6	252	n/a	0.4	0.2	3.0	3.6
		ZN	2.1	266	n/a	0.3	0.6	2.7	3.5
		ZN	1.7	273	n/a	0.3	1.0	0.7	1.9
Post-DIEL	UE-12p#7	VN	2.2	15	259	0	0.0	1.7	1.7
		PW	3.4	29	246	0.7	0.1	3.7	4.2
		SW	8.0	97	183	0.9	0.2	2.6	3.6
		SW	4.1	122	161	0.5	0.5	2.7	3.7
		VN	2.1	146	141	0	0.0	0.8	0.9
		VN	1.8	160	130	0	0.0	1.6	1.6
		VN	1.7	183	109	0	0.0	1.9	1.9
		VN	1.4	222	92	0	0.0	2.5	2.5
		ZN	1.6	249	84	0.1	3.3	1.4	4.8
		ZN	1.7	261	84	0	2.4	0.4	2.7
		ZN	1.9	262	84	0.1	2.4	0.5	2.8
		ZN	1.7	262	84	0	1.8	1.8	3.0
	U12p.03-RE-7	ZN	1.6	3 (258)	56.0	0.4	1.9	1.6	3.7
		ZN	2.2	8 (255)	52.0	0.3	3.0	1.6	5.0
		ZN	1.9	14 (252)	47.4	0.4	2.7	2.5	5.6
		ZN	1.8	19 (250)	44.3	0.1	3.6	2.3	6.0
		ZN	1.4	19 (250)	44.2	0.4	3.3	2.5	6.2
		ZN	1.6	25 (247)	40.4	0.6	4.0	2.2	6.8
		ZN	1.9	32 (243)	36.9	0.7	2.9	3.0	6.6
		ZN	1.5	35 (241)	35.4	0.7	3.4	2.0	6.1
		ZN†	n/a	40 (239)	34.0	3.2	1.6	5.3	10.2

Notes: PW—Partially welded; SW—strongly welded; VN—vitric nonwelded; RL—rhyolitic lava; ZN—zeolitic nonwelded. Pumice aspect ratio was measured as pumice width divided by height.

*Drilling depth is the same as vertical depth except for RE-7 samples; vertical depth is given in parentheses for these samples.

†Sample is distinct from other ZN samples in that it contains no pumice, is highly enriched in phenocrysts, especially biotite, and is likely from the overlying Wahmonie Formation.

due to the intrinsic heterogeneity in the degree of welding within the samples. Intragranular microfractures in post-UNE SW samples are all near the upper limit of pre-UNE levels for both sites. Intragranular microfractures in the VN samples show an increase in intragranular microfracture density from pre- to post-UNE samples at Barnwell. We suspect this may be due to UNE-related compaction, which is described in more detail below in the discussion on VN deformation. This is not the case for VN samples at Disko Elm, where intragranular microfracture densities all lie within pre-UNE levels. The opposite trend is observed for ZN samples: all post-UNE samples at Barnwell lie within pre-UNE levels, and the post-UNE samples at Disko Elm have elevated microfracture densities within 50-m-range distance from the explosive source (Table 3).

Grain-Boundary Microfractures

Post-UNE grain-boundary microfracture densities are greater than those of pre-UNE samples for all units except the VN. The largest increases in post-UNE grain boundary microfracture densities occur within the ZN units at both Barnwell and Disko Elm and in the shallowest PW unit at Barnwell.

DISCUSSION

All lithologies at both locations, with the exception of VN at Disko Elm, show greater microfracture densities in post-UNE samples than in pre-UNE samples. This is true for maximum microfracture densities (Fig. 5) as well as average microfracture densities (Tables 1–2).

Identification of UNE-Induced Damage

Before concluding that the observed differences in microfracture counts arise from the UNE itself, other potential causes of fracturing

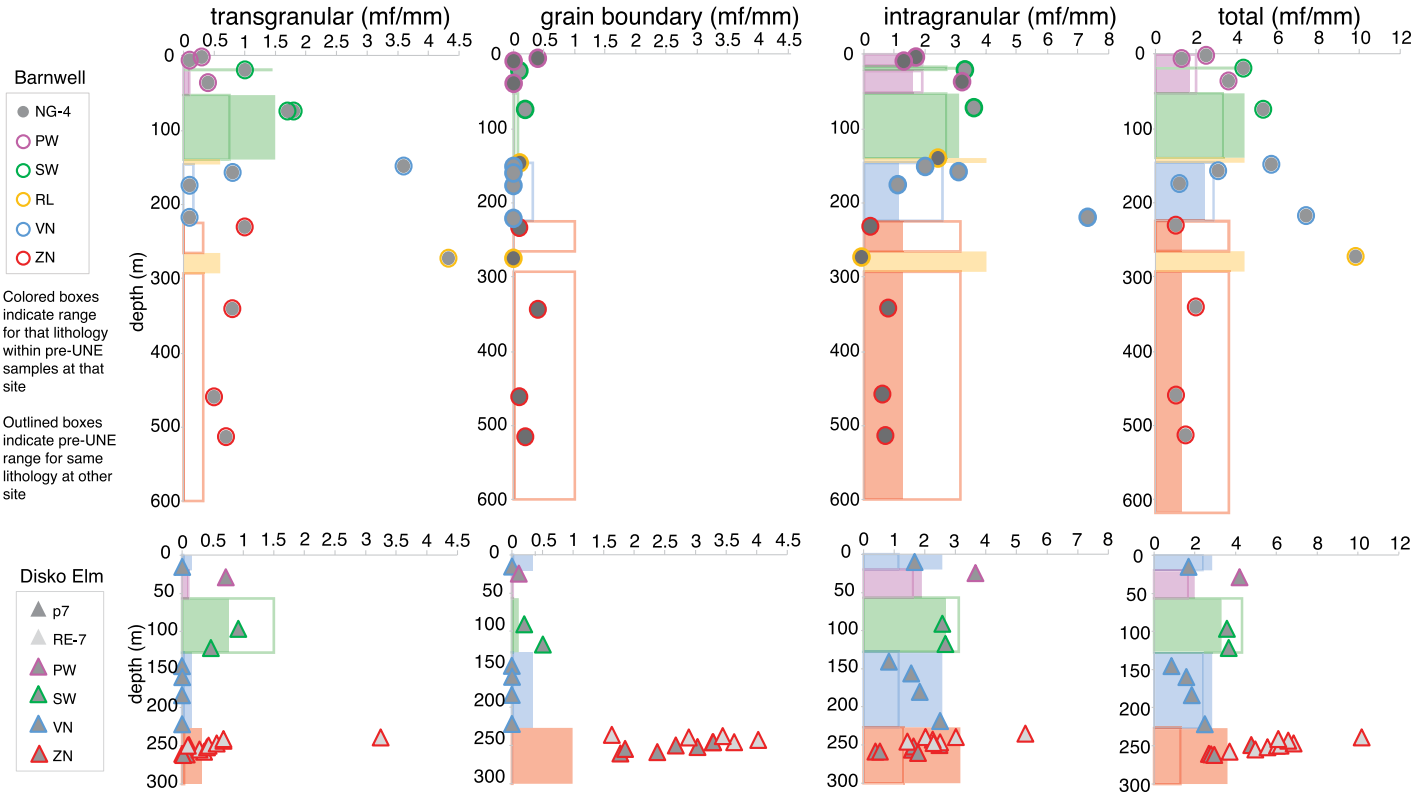

Figure 5. Graphs show microfracture density vs. depth by type of microfracture. Top row, Barnwell site microfractures; circles are post-underground nuclear explosion (UNE) samples. Bottom row, Disko Elm site microfractures; triangles are post-UNE samples. Colored boxes show the range of microfracture values from pre-UNE samples (i.e., location of right edge of box), and they are keyed by lithology in the same colors as the post-UNE samples. The depth extent of the colored boxes shows the lithology distributions of the post-UNE coreholes. The outlined boxes indicate the extent of microfractures from the same lithology at the other UNE site (i.e., the unfilled boxes in the Barnwell site represent microfracture densities for the same lithology at the Disko Elm site, and vice versa, for ease of comparison between sites). Samples with microfracture densities that plot to the right of the boxes are interpreted to have UNE-induced damage.

must be considered. These rocks have experienced a number of different stresses between their formation and our observations. We must consider how these results may be affected by pre-existing variations in microfracture density, and sample collection and handling, before discussing how UNEs produce fractures. These potential confounding factors are discussed below.

Sample Drilling and Handling

There is a potential for drilling to induce microfractures in the rock, thereby complicating the interpretation of potential UNE-induced damage, yet drilling is needed to retrieve samples. We know of no aspect of sample drilling or recovery that could produce the observed patterns of microfractures. Drilling-induced fractures would occur in both pre-UNE and post-UNE samples and would likely involve tensile fractures due to stress concentrations in the wellbore (Kulander et al., 1990). While we do not have information about the specifics of drilling that occurred in the 1960s or 1980s to obtain the pre-UNE samples, we did avoid sampling core where these drilling-induced fractures were observed. All of the post-UNE core has the same diameter as the pre-UNE core, and we know of no major differences in drilling techniques.

Similarly, we do not see differences in microfractures from samples with different handling procedures. One process that could potentially affect the microfracture density is dessication, and some core was wrapped in foil and dipped in wax immediately upon retrieval from the ground, to preserve in situ moisture content. For each set of core samples at Disko Elm, we measured microfracture density from a core that had been preserved in wax and another within the same lithologic unit that had not been preserved in wax (UE-12p#4 at 252 m and 266 m drilling depths, UE-12p#7 at 261 m and 262 m drilling depths, and two samples from U12p.03-RE7 at 19 m drilling depth). We found that the difference in microfracture density of these waxed versus unwaxed samples is negligible (<0.2 mf/mm; refer to Table 3). For Barnwell, all of the pre-UNE samples and all but two post-UNE samples (UE-20az-NG4 at 73 m and 158 m drilling depths) were not wrapped in wax and foil to preserve in situ moisture. These two relatively moist samples have relatively high microfracture densities within their lithologies for both pre-UNE and post-UNE samples. This is the opposite trend from what we would expect if newer samples had more desiccation-induced cracks from differences in handling.

Lastly, all thin sections were made by the same vendor: High Mesa Petrographics. Thus, we would expect no differences in microfractures to result from the creation of the thin sections. In sum, we found no evidence to support the idea that the increase in microfracture densities in post-UNE samples is from drilling or handling.

Are the Pre-UNE Samples Good Textural Matches for the Post-UNE Samples?

Our criteria for determining UNE-induced damage is the presence of more microfractures relative to the maximum of the undamaged samples. The comparison to pre-UNE sam-

ples is dependent on having good analogues for post-UNE samples, or else a change in the number of fractures may represent differences between pre-existing textures instead of explosion-induced damage. Since no core is available from the immediate (<1 km) vicinity of Barnwell that was collected prior to the UNE (which occurred in 1989), our pre-UNE samples are from similar lithologies and determined from thin section observations of mineralogy, welding, and relative amounts of pumice, phenocrysts, and lithic fragments in nearby coreholes. However, these samples come from distances of 5–18 km and may not match the geologic unit or depth. In addition, the textures are not always identical to the post-UNE samples, but they are the best available matches. Because of this, some degree of uncertainty exists when comparing pre-UNE to post-UNE samples, particularly at Barnwell.

Based on a comparison of petrographic features and relative amounts of groundmass, phenocrysts, pumice, and lithic fragments by petrographic point counting (Table 1; Fig. 3), the poorest analogue among Barnwell samples occurs for the RL lithology. This unit is distinguishable by its vitric matrix, with pre-UNE RL consisting of pumice, glass shards, and glassy lithic fragments, and post-UNE RL consisting of massive glass matrix with relatively rare phenocrysts and lithic fragments. Thus, the difference in transgranular fractures from 2 mf/mm to 4 mf/mm pre-UNE RL and ~10–20 mf/mm post-UNE RL is not likely to represent explosion-induced damage, but more likely represents the extent to which hydration-related fracturing occurred in the more massive matrix of the post-UNE RL unit. Fortunately, other lithologies have much better matches between pre-UNE and post-UNE samples (Table 1) such that comparisons are valuable.

For Disko Elm, we obtained pre-UNE analogue samples from a closer location just 150 m away. A comparison of microtextural features with those of post-UNE samples, along with a comparison of relative amounts of tuff components via petrographic point counting (Table 2), shows that these are excellent analogs. Thus, the differences between pre-UNE and post-UNE microfracture densities are less likely to be the result of natural variation in the rock. However, these samples still contain variability in microfracture density. This may be the reason behind the post-UNE VN samples having fewer microfractures (0.9–2.5 mf/mm) than pre-UNE samples (1.0–2.9 mf/mm; see Fig. 5, where VN is the only lithology to have no post-UNE data points outside the pre-UNE range). This particular lithology is the most variable in terms of grain sizes, grain-contact area, and porosity—properties that affect the strength of the tuff (Moon, 1993; Wilson et al., 2003b), which in turn can determine whether a through-going fracture will propagate (Martin et al., 1993; Wilson et al., 2003b).

We have identified the best sets of pre-UNE and post-UNE samples with which to evaluate the effect of a UNE on microscale damage from source to surface, and with those, we see a subtle increase from pre-UNE to post-UNE samples. However, we still see variability in microfracture density in the pre-UNE RL and VN samples, which complicates the interpretation of UNE-induced damage in these units.

The Extent of UNE-Induced Damage

The UNE-induced damage, as defined by increases in microfracture density relative to pre-shot analogues, appears to be strong within ~50 m of the center of the explosion in the case of Disko Elm and decreases with range distance (Fig. 6), as expected based on previous work (Borg, 1973; Carroll, 1983). However, we also observe a more subtle increase in microfracture densities at larger distances (in every lithology except VN), which is not consistent with previous work.

Predictions from many numerical models (e.g., Terhune, 1971; Carroll, 1983; Sammis, 1991; Pawloski, 1999; Sammis, 2004) largely do not predict that fracturing should occur at these large distances from the UNE source. These models generally predict damage to ~1/5 the depth of burial, which would not extend to the range distances where we are seeing microdamage. However, these models are calibrated against data types that are favored for the ease of collection, such as obvious visual disturbance and changes in seismic velocity. This leaves the details or outliers unexplained. These reported damage extents are at a macroscopic scale, with very few exceptions: in sandstones and shales (Borg, 1970), in granite (Short, 1966), and in salt and basalt (Short, 1968). None of these are in tuff. Thus, the more limited extent of damage from the models and the mesoscale observations may not be inconsistent with a larger microscale damage extent. We argue that the smaller-scale details help us see the mesoscale observations plus the unexplained/unseen damage, which gives a more

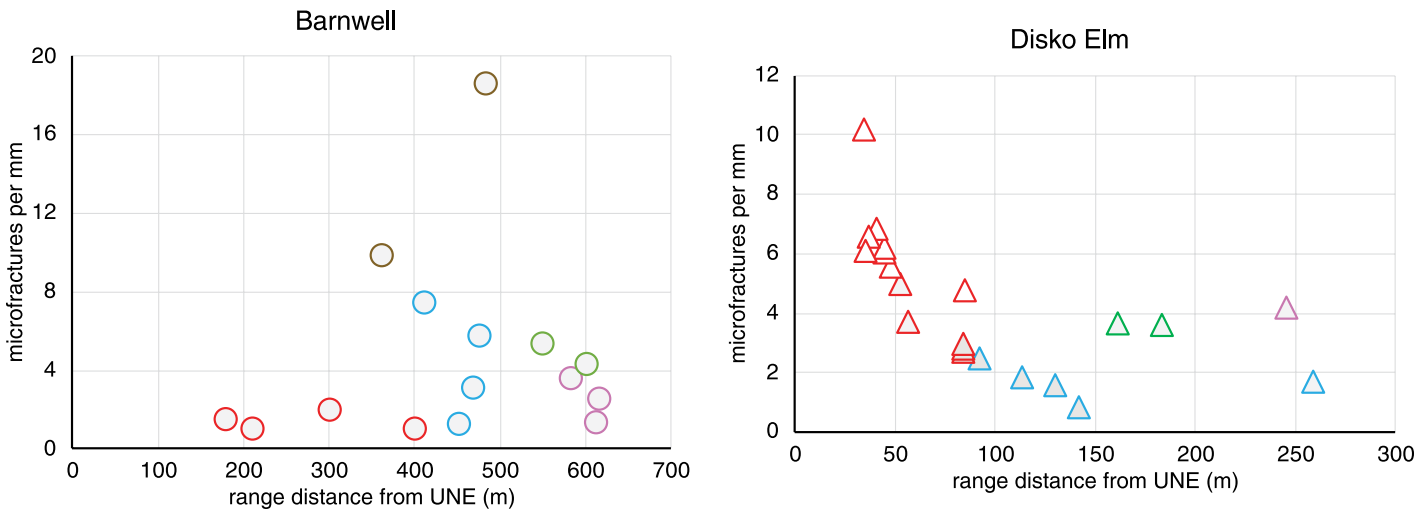

Figure 6. Total microfracture densities vs. range distance from underground nuclear explosions (UNEs). Circles indicate post-Barnwell samples, and triangles indicate post-Disko Elm samples. Symbols are color keyed by lithology: red—ZN; blue—VN; brown—RL; green—SW; and purple—PW.

complete understanding of how UNEs may affect the heterogeneous subsurface.

Unlike most UNE studies, a study using quantified microfractures to determine damage induced from an underground chemical explosion in granite (Swanson et al., 2018) did show some evidence of source-to-surface damage, although it was subtle. In that study, the most obvious microfracture damage (and all observable core-scale damage) occurred within a near-source damage zone (~10 m from the source) and spall-related damage at the surface. Thus, based on previous work, it seems possible that microfractures may indicate larger extents of damage than the modeling predicts.

There are a few studies that suggest that microdamage at longer range distances may be expected. A model by Johnson and Sammis (2001) predicts damage out to scaled distances that approximate the burial depth of these sites. Adushkin and Spivak (2004) present changes in seismic velocity that are continuous to the surface, but not in tuff. They see these changes to a scaled range distance of 120 m/kt$^{1/3}$, at which point the longitudinal velocities approach that of the undisturbed rock. This scaled distance is derived from "seismic radiographic inspection," defined by changes in velocity, of rock that is less porus than tuff. If we were to employ this scaled distance to predict the extent of damage using the maximum of the announced yield range, we would predict an extent of damage of 326 m for Disko Elm and 638 m for Barnwell. These values approximate the burial depth, and these ranges would include nearly all of the samples we collected.

Thus, the damage we observe here, with a subtle region of damage over the entire burial depth and a more damaged region closer to the explosive source, is consistent with a few previous studies but is largely not expected from previous work.

The Nature of UNE-Induced Damage

Interpretations of Damage, by Lithology

The tuff sequences at Barnwell and Disko Elm are composed of individual cooling units, which vary in their degree of welding (quantified in this study by pumice aspect ratio) and post-depositional crystallization. These lithologies form a subhorizontal anisotropy through which UNE-damage is expected to vary due to differences in material properties (Table 1). From previous studies of fault-zone and experimental deformation in ash-flow tuffs in the shallow subsurface (~<600 m), we expect to see the degree and nature of fracturing to be controlled by lithology. Essentially, welding and postdepositional crystallization typically decrease porosity and increase the area and strength of grain contacts, providing a rigid framework through which fractures may propagate. Therefore, in a relatively shallow volcanic tuff sequence with these conditions, we expect low-porosity welded units to deform by fracture at the microscale and the mesoscale, with fracture density increasing with the degree of welding and relative amount of flattened pumice (Soden et al., 2016). High-porosity vitric, nonwelded units are expected to deform by cataclasis within deformation bands (Wilson et al., 2003b; Evans and Bradbury, 2004). Moderately porous nonwelded units that have undergone postdepositional crystallization may form either deformation bands or fractures, depending on local variations in the degree and nature of crystallization, grain-size distributions, and bed thickness (Wilson et al., 2003b; Dinwiddie et al., 2012).

For the tuff sequences at Barnwell and Disko Elm, the degree of post-UNE increase over pre-UNE microfracture densities appears to be controlled largely by welding and composition, with strongly and partially welded samples containing larger numbers of microfractures at both sites for all types of microfractures. Nonwelded samples contain no observed deformation bands, but evidence of grain rearrangement and densities of impingement microfractures show that UNE damage in these layers is controlled by textural variations (pumice vs matrix content, microporosity, etc.). Microstructural details for all lithologic units, each of which defines a subhorizontal layer of varying material properties, are given below and in Tables 1–3.

Partially welded (PW). PW units in this study were nearly completely crystallized with only incipient welding and contained only fractures. Between the two shallow (<10 m drill depth), post-Barnwell PW samples, the degree of welding and microfracture density are inversely correlated. For the deeper post-Barnwell and two pre-Barnwell samples, the degree of welding and microfracture density are positively correlated. This suggests that small variations in welding within the PW unit do not follow the expected relationship with microfracture density, even when UNE damage is not involved. That is, the natural damage pattern in the pre-UNE samples does not match the natural damage patterns found in tectonic studies. This is a bit puzzling but may be due to some other material property influencing microfracture density in these samples, perhaps the nature and degree of crystallization.

Comparing the pre-UNE to post-UNE PW samples from Barnwell, microfracture densities are larger in the post-UNE samples, which suggests UNE-induced damage. This increase in microfractures apparently overcomes the pre-existing variability in the degree of welding among samples.

The post-UNE PW sample at Disko Elm also has a larger microfracture density than the pre-UNE PW sample (Table 3, Fig. 5). At this location, the degree of welding is essentially the same in pre- and post-UNE PW samples and therefore would not be expected to affect microfracture densities. These PW rocks are from a shallow unit and therefore further from the UNE source at both sites. Considering the location of these samples, we suspect spallation processes, where the shock wave interacts with the ground surface (e.g., Khalturin et al., 2005; Jordan et al., 2015), may have induced the observed fracturing in PW samples.

Strongly welded (SW). In the SW samples, we observe a positive correlation between welding and microfracture density, where more strongly welded samples have greater numbers of microfractures. This is expected from studies in naturally deformed environments. Induration due to fusion and compaction of all pumice and matrix components allows deformation via extensive transgranular microfracturing (Figs. 4D–4F and 5). We observe significantly more transgranular microfractures in SW units than in PW units at both locations, which is also expected.

At Barnwell, microfracture densities are slightly higher in post-UNE samples than in pre-UNE samples. However, it is less clear if this is a result of damage from the UNE. Within each set of pre-UNE or post-UNE samples, higher microfracture densities correlate with a higher degree of welding. The average degree of welding, as defined by pumice aspect ratio, is higher in the post-UNE set than the pre-UNE set (Table 1). Therefore, the apparent increase in microfractures between pre-UNE and post-UNE samples may result from differences in texture and pre-existing fractures. Among Barnwell SW samples, both microfracture density and the degree of welding increase with sample depth. Thus, it is unclear whether that downward increase is from natural pre-existing variation or due to increased fracturing with proximity to the UNE source, which is hundreds of meters away from these samples.

Post-UNE SW samples at Disko Elm have larger microfracture densities than pre-UNE SW samples. The degrees of welding and unit thicknesses are similar for both pre-and post-UNE SW samples, which suggests that the UNE contributes to microscale damage in this unit.

Rhyolitic lava and vitrophyre (RL). Although the RL unit at Barnwell is poorly matched with pre-UNE analogs, we can expand on the microstructures observed and implications for deformation mechanisms in this post-UNE

vitric unit. Since the RL samples are indurated, we expected to observe higher densities of microfractures, particularly transgranular ones, relative to less indurated units. We do observe large microfracture densities, higher than the strongly welded units above, with the transgranular microfractures being the most numerous (Fig. 5). Microfractures observed in this unit have predominantly small apertures (1–5 μm), with several curved microfractures branching from a single microfracture and commonly terminating within a millimeter of the branch point (i.e., most microfractures are not through-going within a sample; Figs. 4G–4I). The morphology of these microfractures suggests that they formed as a result of hydration during cooling of the lava (McPhie et al., 1993; Gimeno et al., 2003) and may not be an indication of UNE-related deformation. However, as explained earlier in the discussion, we do not have an appropriate pre-UNE analogue for this highly microfractured unit, so we don't know if these microfractures were present but in lesser amounts before the UNE test.

Vitric, nonwelded (VN). In VN samples from both locations, microfracture densities are generally low, as expected from previous work, but quite variable. Microfracture densities in this lithology have different patterns at the two sites. At Barnwell, post-UNE microfracture densities are all well above the pre-UNE sample values for all microfracture types except for grain boundary, where they are equal and total zero. However, at Disko Elm, post-UNE microfracture densities are still within the pre-UNE range for all microfracture types. Therefore, the number of microfractures in this lithology may not fully reflect UNE-induced damage. Instead, the microfracture densities appear to be controlled by lithologic variations. In most VN thin sections, there is little to no grain-contact area, and microfracture densities, especially transgranular microfracture densities, are very low. However, in some thin sections, individual glass shards, lithic clasts, phenocrysts, and pumice were observed to be compacted just enough to increase grain-contact area, which allowed impingement cracks to form (Figs. 4J–4L).

We hypothesize that the lack of UNE-induced increase in microfracture density in the VN unit at Disko Elm may be due to more grain rearrangement (sliding, rotation, and pore space reduction) prior to fracturing at Disko Elm than at Barnwell. This is likely due to variations in grain sorting in these units. At both locations, stronger components (phenocrysts, lithic fragments, and pumice) are supported in a matrix of nonwelded ash and glass shards. There is only one VN sample that is not matrix-supported: Barnwell post-UNE sample at 220.1 m, which is phenocryst and pumice-supported with very little matrix (and it has an abnormally high microfracture density, likely for that reason). At Disko Elm, the stronger components are more abundant than the groundmass (Table 2) but still supported by that matrix, which results in a more poorly sorted assemblage that allows for more grain sliding, rotation, and collapse of pore space before fracturing occurs (e.g., Skurtveit et al., 2013). At Barnwell, the relatively large amount of groundmass and smaller pumice sizes reduce this effect. This grain rearrangement, which could be more significant at Disko Elm, can act to absorb the explosive energy from the UNE without creating new microfractures. This behavior, although difficult to quantify, is important to incorporate when modeling UNE damage, because these poorly characterized units could be partly shielding the shock-wave energy from overlying units and the surface, which may affect the outgoing pulse shapes and ground motion during the monitoring of UNEs (e.g., Fourney et al., 1993, 1994).

Pore collapse, in the form of pore-surrounding fractures or full-scale collapse with material filling pores, was not commonly observed. Some pores, especially unbroken pumice vesicles, were filled with broken material but with no definitive evidence that this was a result of postdepositional cataclasis (Figs. 4J–4K). Microporosity data from pre- and post-UNE samples can provide an estimate of grain rearrangement and pore compaction in the absence of microfractures. In all pre- and post-UNE VN sample pairs, microporosity decreases for the post-UNE sample range from 3% to 10% (Tables 1–2). While this decrease in porosity is small and based on data from one representative sample in each VN unit, it may indicate that pore compaction and grain rearrangement occurred without producing any directly observable indicators of damage, as invoked by others to explain their experimental sand compaction results (e.g., Karner et al., 2005; Skurtveit et al., 2013)

Zeolitic, nonwelded (ZN). In ZN units, post-UNE samples have larger numbers of microfractures, especially grain-boundary microfractures, at both the Barnwell and Disko Elm sites (Figs. 4M–4O and 5). At Disko Elm, there is a prominent trend of increasing fractures with decreasing distance from the UNE source (Fig. 6). This trend is not a function of depth, as RE-7 was drilled upwards to approach the source, and UE-12p#7 was drilled vertically downward toward the source (see Fig. 2). This strongly supports the interpretation that many of these microfractures were created by the UNE. Total microfracture densities for post-UNE samples are all above or at the high end of the pre-UNE range, which suggests that microfracture density is influenced by UNE damage. At Barnwell, we observe more intense microscale deformation in the form of pore collapse and the crushing of postdepositional crystal-fill in some pumice voids in only the deepest (516 m drilling depth) sample, but there is no increase in post-UNE microfracture densities with depth (i.e., proximity to the UNE).

All microfractures in the pre-UNE ZN sample at Barnwell are intragranular, whereas post-UNE microfractures consist of intragranular, transgranular, and grain-boundary varieties. This suggests that UNE damage may create different types of microfractures than the pre-existing tectonic type and may indicate a potential way to distinguish explosion-induced damage from tectonic damage, at least in some ZN rocks. However, these other microfracture types are found in pre-UNE Disko Elm samples, so this requires further study before it can be used as an indicator of UNEs.

At Disko Elm, most post-UNE ZN microfracture densities are higher than the pre-UNE values. The degree of zeolitization varies, primarily increasing with depth in both pre- and post-UNE samples, with minor variations. As the degree of zeolitization increases, total microfracture density also increases. For example, the few post-UNE samples that have total microfracture densities in the pre-UNE range are those samples with some vitric content remaining. For ZN samples containing no glass, total microfracture density correlates with zeolite crystal growth and interconnectivity, especially within the ~50-m-range distance of the UNE.

Within this 50-m-damage zone, range distance is not the only factor controlling the microfracture densities of Disko Elm samples. For example, microfracture densities at the 36.9 m and 35.4 m range distances are lower than those of the neighboring samples. These samples have more groundmass (composed of matrix material) than pumice or phenocrysts than the adjacent, more microfractured samples. So, even within a distinctly defined damage zone, lithologic properties still appear to influence the degree of deformation.

If we also consider the relative densities of each type of microfracture in samples at Disko Elm, we see that post-UNE, transgranular microfracture densities increase with proximity to the UNE within ~50-m-range distance of the UNE, which possibly marks the zonation of damage associated with the UNE. Post-UNE grain-boundary microfracture densities are consistently above the pre-UNE range for the entire ZN unit from Disko Elm. Some of these post-UNE samples have up to four times the

number of grain-boundary microfractures than the pre-UNE sample with the highest density of this microfracture type. This suggests that grain-boundary microfracturing is the main UNE-induced deformation mechanism active in this unit both within and beyond the 50-m-range distance surrounding the UNE source. Grain boundary fractures are not as common at the Barnwell site, although they are clearly above the background value of 0.

Interpretations of Damage, by Range Distance

Understanding the effects of lithology on fracture patterns is complicated by the dynamic regimes around UNEs. For both of these UNEs, the explosions were centered in the ZN lithology. In addition, the shallow units, where spall damage would occur, primarily consist of the PW and SW units. The most noticeable trend regarding range distance is the increase in microfracture density with decreasing range distance, which occurs within 50 m of Disko Elm (Fig. 6).

Near-source (<50-m-range distance from UNE): At Disko Elm, samples collected from near the UNE source showed high numbers of grain boundary fractures and moderately high numbers of transgranular and intragranular microfractures, as compared with pre-UNE samples. This regime is expected to be damaged via very large peak stresses. At Barnwell, where the closest samples were still 188 m away from the source, there is an apparent increase in the intensity of microdamage in the closest samples and more grain-boundary fractures relative to the pre-Barnwell samples but not to the pre-Disko Elm equivalents.

These results are consistent with findings by Martin et al. (1993), who compared microstructural characteristics in pre- and post-UNE zeolitic, nonwelded tuff from other cores near Disko Elm. Similar to our results, they find that the frequency of microfractures appeared to be a function of both the proximity to the source and the material composition. They also interpret that shock (dynamic) loading damage structure could be overshadowed by the effects of mineralogy and initial high porosity of the tuff, particularly at longer range distances, although they did not examine samples from the longer distances we studied here. They also found that UNE damage (but not lab-induced damage to samples that experienced the same peak stress) was largely homogeneously distributed, with no signs of incipient localization. Since they only studied the ZN component of the rock, our results are the first to indicate that the influence of pre-existing texture is strong among all lithologic groups above this UNE. In addition, our results show that a lack of localization occurs within all lithologic units, as we found no deformation bands, even among units that tend to form deformation bands under tectonic stresses (i.e., the VN samples).

Deformation Mechanisms

Our finding of increased microfracture densities for all lithologies following UNEs, with the exception of VN at Disko Elm, raises some interesting questions. The first is why VN samples at Disko Elm don't show damage, when samples neighboring those with other textures do show damage. One potential explanation is that the damage isn't there. A second potential explanation is that damage is there, but we can't see it in the microfracture counts.

The locations of the VN samples make the first option possible: they are between the near-source ZN samples and the near-surface PW, SW, and potentially RL samples that may have experienced destructive interference between the direct stresses and the stresses reflected off the surface (spall). Since the VN samples sit in this same relative location at both Barnwell and Disko Elm, this possibility cannot be ruled out. However, VN samples have, by far, the lowest strengths (Broome et al., 2019), so it would be odd for the surrounding textures to deform at higher stresses and not induce damage in VN samples.

The second option is that the VN samples deform by mechanisms other than microfracturing. This interpretation is supported by previous work showing that vitric, nonwelded rocks tend to deform in deformation bands instead of fractures, which contains grain-scale fracturing and pore collapse (e.g., Wilson et al., 2003b). While some collapsed pores were observed in these VN samples, they were not widespread. Microporosity data is suggestive of some pore collapse (post-UNE samples have microporosity values ∼20% lower; Table 2), but the data are too limited for a definitive interpretation. In addition, deformation bands were not observed.

The lack of deformation bands is puzzling, and some work suggests that in post-UNE samples, this may result from the high loading strain rates. The high strain rates associated with UNEs may preferentially induce distributed, over localized damage (Martin et al., 1993), and release more flaws and releasing more energy than tectonic damage (Grady and Kipp, 1993; Zwiessler et al., 2017), particularly in porous materials (Buhl et al., 2014). However, an explanation due to high strain rates would not explain the lack of deformation bands in the pre-UNE samples. This lack of deformation bands in pre-UNE VN samples remains enigmatic, especially since deformation bands are observed in the field in the VN lithologies of neighboring units (Sweetkind and Drake, 2007). We suspect that widely spaced deformation bands exist in these VN units, but our sampling missed them. Thus, it remains unclear why the VN samples show so little damage from the UNE. Future work will be needed to resolve how this porous, weak rock accommodates damage.

CONCLUSIONS

We find that a slightly higher microfracture density is present in most post-UNE samples compared to pre-UNE samples, even at much greater distances from the explosive source than was previously considered. A distinctly larger number of microfractures, particularly grain-boundary and intragranular microfractures, occurs within 50 m of Disko Elm. Outside of this close range, damage continues in a more subtle manner all the way up to the near-surface samples. However, for most locations, the increase over pre-UNE samples is small (usually less than two times the pre-UNE average) and requires the pre-UNE comparison samples to be a very good match, both texturally and compositionally. For these more distal samples, the degree of UNE-induced damage appears to be controlled largely by sample texture, with strongly and partially welded samples containing larger numbers of microfractures at both sites for all types of microfractures.

For vitric, nonwelded samples, only one of the two sites shows an increase in microfractures over pre-UNE equivalents. Despite the lack of apparent UNE-induced fractures in the Disko Elm vitric, nonwelded samples, these samples do show a reduction in microporosity. Thus, damage may be accommodated in these samples at a scale even smaller than can be observed from thin sections, such as in a distributed manner. The subtle nature of deformation in this unit requires further study to understand its mechanisms. Damage in the Disko Elm vitric, nonwelded samples do not manifest as large, continuous fractures, as is currently modeled (e.g., Carrigan et al., 2020).

Shock-induced microfractures manifest more commonly as grain boundary and transgranular microfractures, particularly near the source. These types of fractures would be more likely to increase the transport of radionuclides than either smaller intragranular fractures or pore crush. The extent to which lithology affects near-source deformation mechanisms remains unclear, as we were only able to examine rocks from explosions in zeolitic, nonwelded tuffs.

We argue that deformation is dependent on the varying material properties, both within and between lithologies, as well as the distance

from the UNE source. At these sites, damage manifests as a subtle increase in microfracture density for most locations in the subsurface and more significant damage within ~50 m of the UNE. The weakest material at middle depths, vitric, nonwelded tuff, is affected by the UNE in a way that is difficult to quantify. In any case, the nature, quantity, and extent of microfractures affects both the continued stress propagation into the overlying units, as well as gas migration through the rock, and need to be considered in future modeling efforts.

ACKNOWLEDGMENTS

The Underground Nuclear Explosion Signatures Experiment (UNESE) was created to apply a broad range of research and development (R&D) techniques and technologies to nuclear explosion monitoring and nuclear nonproliferation. It is a multi-year research and development project sponsored by the National Nuclear Security Administration, Defense Nuclear Nonproliferation Research and Development (NNSA DNN R&D), and is collaboratively executed by Lawrence Livermore National Laboratory, Los Alamos National Laboratory, Mission Support and Test Services, Pacific Northwest National Laboratory, and Sandia National Laboratories. Los Alamos National Laboratory is operated by Triad National Security, LLC, for the National Nuclear Security Administration of the U.S. Department of Energy (contract no. 89233218CNA000001). LA-UR-21-23998. Sandia National Laboratories is a multi-mission laboratory managed and operated by National Technology and Engineering Solutions of Sandia, LLC, a wholly owned subsidiary of Honeywell International, Inc., for the U.S. Department of Energy's National Nuclear Security Administration under contract DE-NA0003525 SAND2022-8458 J.

REFERENCES CITED

Adushkin, V.V., and Spivak, A.A., 2004, Changes in properties of rock massifs due to underground nuclear explosions: Combustion, Explosion, and Shock Waves, v. 40, no. 6, p. 624–634, https://doi.org/10.1023/B:CESW.0000048263.34894.58.

Anders, M.H., Laubach, S.E., and Scholz, C.H., 2014, Microfractures: A review: Journal of Structural Geology, v. 69, Part B, p. 377–394, https://doi.org/10.1016/j.jsg.2014.05.011

Borg, I.Y., 1970, Microfracturing in Postshot Gasbuggy Core GB-3: Lawrence Radiation Laboratory Report UCRL-50893, 15 p.

Borg, I.Y., 1973, Extent of pervasive fracturing around underground nuclear explosions: International Journal of Rock Mechanics and Mining Sciences, v. 10, p. 11–18, https://doi.org/10.1016/0148-9062(73)90056-9.

Bourret, S.M., Kwicklis, E.M., Miller, T.A., and Stauffer, P.H., 2019, Evaluating the importance of barometric pumping for subsurface gas transport near an underground nuclear test site: Vadose Zone Journal, v. 18, https://doi.org/10.2136/vzj2018.07.0134.

Broome, S.T., Wilson, J.E., Swanson, E.M., Sussman, A.J., Jaramillo, J., and Barrow, P., 2019, Material property determinations of P-tunnel core in support of UNESE: Albuquerque, New Mexico, Sandia National Lab, SAND2019-13649, 68 p.

Buhl, E., Poelchau, M., Dresen, G., and Kenkmann, T., 2014, Scaling of sub-surface deformation in hypervelocity impact experiments on porous sandstone: Tectonophysics, v. 634, p. 171–181, https://doi.org/10.1016/j.tecto.2014.07.030.

Burkhard, N.R., and Wagoner, J.L., 1989, U20az site characteristics report: Livermore, California, Lawrence Livermore National Laboratory, Internal Memorandum CP 89-67, 38 p.

Carrigan, C.R., and Sun, Y., 2014, Detection of noble gas radionuclides from an underground nuclear explosion during a CTBT on-site inspection: Pure and Applied Geophysics, v. 171, no. 3–5, p. 717–734, https://doi.org/10.1007/s00024-012-0563-8.

Carrigan, C.R., Heinle, R.A., Hudson, G.B., Nitao, J.J., and Zucca, J.J., 1996, Trace gas emissions on geological faults as indicators of underground nuclear testing: Nature, v. 382, p. 528–531, https://doi.org/10.1038/382528a0.

Carrigan, C.R., Sun, Y., Hunter, S.L., Ruddle, D.G., Simpson, M.D., Obi, C.M., Huckins-Gang, H.E., Prothro, L.B., and Townsend, M.J., 2020, Gas transport across the low-permeability containment zone of an underground nuclear explosion: Scientific Reports, v. 10, 1437, https://doi.org/10.1038/s41598-020-58445-1.

Carroll, R.D., 1983, Seismic velocities and postshot properties in and near chimneys, *in* Jones, E., ed., Proceedings, Monterey Containment Symposium, Monterey, California, LA-9211-C, Volume 1: Los Alamos, New Mexico, Los Alamos National Laboratory, p. 379–396.

Carroll, R.D., and Lacomb, J.W., 1993, Borehole techniques identifying subsurface chimney heights in loose ground–some experiences above underground nuclear explosions: International Journal of Rock Mechanics and Mining Sciences & Geomechanics Abstracts, v. 30, no. 6, p. 575–590, https://doi.org/10.1016/0148-9062(93)91218-8.

Chipera, S.J., Goff, F., Goff, C.J., and Fittipaldo, M., 2008, Zeolitization of intracaldera sediments and rhyolitic rocks in the 1.25 Ma lake of Valles caldera, New Mexico, USA: Journal of Volcanology and Geothermal Research, v. 178, p. 317–330, https://doi.org/10.1016/j.jvolgeores.2008.06.032.

Dinwiddie, C.L., Bradbury, K.K., McGinnis, R.N., Stillman, D.E., and Ferrill, D.A., 2012, Hydrogeologic heterogeneity of faulted and fractured Glass Mountain bedded tuffaceous sediments and ash-fall deposits: The Crucifix site near Bishop, California: Lithosphere, v. 4, no. 1, p. 40–62, https://doi.org/10.1130/L179.1.

Dwivedi, S.K., Asay, J.R., and Gupta, Y.M., 2006, Two-dimensional mesoscale simulations of quasielastic reloading and unloading in shock compressed aluminum: Journal of Applied Physics, v. 100, 083509, https://doi.org/10.1063/1.2357415.

Espinosa, H.D., and Zavattieri, P.D., 2003, A grain level model for the study of failure initiation and evolution in polycrystalline brittle materials. Part I: Theory and numerical implementation: Mechanics of Materials, v. 35, p. 333–364, https://doi.org/10.1016/S0167-6636(02)00285-5.

Evans, J.P., and Bradbury, K.K., 2004, Faulting and fracturing of nonwelded Bishop Tuff, Eastern California: Deformation mechanisms in very porous materials in the Vadose Zone: Vadose Zone Journal, v. 3, p. 602–623, https://doi.org/10.2136/vzj2004.0602.

Fensin, S.J., Cerreta, E.K., Gray, G.T., III, and Valone, S.M., 2014, Why are some interfaces in materials stronger than others?: Scientific Reports, v. 4, https://doi.org/10.1038/srep05461.

Fourney, W.L., Dick, R.D., and Weaver, T.A., 1993, Explosive shielding by weak layers: Los Alamos, New Mexico, Los Alamos National Lab, LA-UR-93-224.

Fourney, W.L., Dick, R.D., Taylor, S.R., and Weaver, T.A., 1994, An analysis of three nuclear events in P-tunnel: Los Alamos, New Mexico, Los Alamos National Lab, LA-UR-94-1750.

Gale, J.F.W., and Gomez, L.A., 2007, Late opening-mode fractures in karst-brecciated dolostones of the Lower Ordovician Ellenburger Group, west Texas: Recognition, characterization, and implications for fluid flow: AAPG Bulletin, v. 91, no. 7, p. 1005–1023, https://doi.org/10.1306/03130706066.

Gibbons, A.B., Hinrichs, E.N., Hansen, W.R., and Lemke, R.W., 1963, Geologic map of the Rainier Mesa quadrangle, Nye County, Nevada: U.S. Geological Survey Map GQ-215, scale 1:24,000.

Gimeno, D., Diaz, N., Garcia-Valles, M., and Martinez-Manent, S., 2003, Genesis of bottom vitrophyre facies in rhyolitic pyroclastic flows: A case study of syneruptive glass welding (Nuraxi unit, Sulcis, SW Sardinia, Italy): Journal of Non-Crystalline Solids, v. 323, p. 91–96, https://doi.org/10.1016/S0022-3093(03)00295-3.

Grady, D.E., and Kipp, M.E., 1993, Dynamic fracture and fragmentation, *in* Asay, J.R., and Shahinpoor, M., eds., High-Pressure Shock Compression of Solids: New York, Springer, p. 265–322, https://doi.org/10.1007/978-1-4612-0911-9_8.

Heath, J., Kuhlman, K., Broome, S., Wilson, J., and Malama, B., 2021, Heterogeneous multiphase flow properties of volcanic rocks and implications for noble gas transport from underground nuclear explosions: Vadose Zone Journal, v. 20, https://doi.org/10.1002/vzj2.20123.

Huckins-Gang, H. and Townsend, M., 2018, Drilling, completion, and geologic characterization of core hole U12p.03 RE-7, U12p tunnel, Aqueduct Mesa, Nevada National Security Site: Mission Support and Test Services Report.

Johnson, L.N., and Sammis, C.G., 2001, Effects of rock damage on seismic waves generated by explosions: Pure and Applied Geophysics, v. 158, p. 1869–1908, https://doi.org/10.1007/PL00001136.

Jordan, A.B., Stauffer, P.H., Knight, E.E., Rougier, E., and Anderson, D.N., 2015, Radionuclide gas transport through nuclear explosion-generated fracture networks: Scientific Reports, v. 5, https://doi.org/10.1038/srep18383.

Karner, S.L., Chester, J.S., Chester, F.M., Kronenberg, A.K., and Hajash, A., Jr., 2005, Laboratory deformation of granular quartz sand: Implications for the burial of clastic rocks: AAPG Bulletin, v. 89, no. 5, p. 603–625, https://doi.org/10.1306/12200404010.

Khalturin, V.I., Rautian, T.G., Richards, P.G., and Leith, W.S., 2005, A review of nuclear testing by the Soviet Union at Novaya Zemlya, 1955–1990: Science & Global Security, v. 13, no. 1–2, p. 1–42, https://doi.org/10.1080/08929880590961862.

Kulander, B.R., Dean, S.L., and Ward, B.J., Jr., 1990, Fractured Core Analysis. Interpretation, Logging, and Use of Natural and Induced Fractures in Core: Tulsa, Oklahoma, American Association of Petroleum Geologists, Methods in Exploration Series 8, 88 p.

Lange, D.A., Jennings, H.M., and Shah, S.P., 1994, Image analysis techniques for characterization of pore structure of cement-based materials: Cement and Concrete Research, v. 24, no. 5, p. 841–853, https://doi.org/10.1016/0008-8846(94)90004-3.

Lowrey, J.D., Biegalski, S.R., and Deinert, M.R., 2013, UTEX modeling of radioxenon isotopic fractionation resulting from subsurface transport: Journal of Radioanalytical and Nuclear Chemistry, v. 296, p. 129–134, https://doi.org/10.1007/s10967-012-2026-1.

Martin, J.W., Fredrich, J.T., Felice, C.W., and Green, S.J., 1993, Mechanical properties and microstructure of shock-conditioned tuff: International Journal of Rock Mechanics and Mining Sciences & Geomechanics Abstracts, v. 30, no. 7, p. 669–675, https://doi.org/10.1016/0148-9062(93)90003-V.

McPhie, J., Doyle, M., and Allen, R., 1993, Volcanic Textures: A Guide to the Interpretation and Textures in Volcanic Rocks: Hobart, Australia, University of Tasmania Center for Ore Deposit and Exploration Studies, 198 p.

Mitchell, T.M., and Faulkner, D.R., 2009, The nature and origin of off-fault damage surrounding strike-slip fault zones with a wide range of displacements: A field study from the Atacama fault system, northern Chile: Journal of Structural Geology, v. 31, p. 802–816, https://doi.org/10.1016/j.jsg.2009.05.002.

Moncure, G.K., Surdam, R.C., and McKague, H.L., 1981, Zeolite diagenesis below Pahute Mesa, Nevada Test Site: Clays and Clay Minerals, v. 29, no. 5, p. 385–396, https://doi.org/10.1346/CCMN.1981.0290508.

Moon, V., 1993, Microstructural controls on the geomechanical behavior of ignimbrite: Engineering Geology, v. 35, p. 19–31, https://doi.org/10.1016/0013-7952(93)90067-M.

Ogilvie, P., Gibson, R.G., Reimold, W.U., Deutsch, A., and Hornemann, U., 2011, Experimental investigation of shock metamorphic effects in a metapelitic granulite:

The importance of shock impedance contrast between components: Meteoritics & Planetary Science, v. 46, no. 10, p. 1565–1586, https://doi.org/10.1111/j.1945-5100.2011.01250.x.

Pawloski, G.A., 1999, Development of phenomenological models of underground nuclear tests on Pahute Mesa, Nevada Test Site—BENHAM and TYBO: Lawrence Livermore National Laboratory Report UCRL-ID-136003, 46 p.

Perez, R.J., and Boles, J.R., 2005, Interpreting fracture development from diagenetic mineralogy and thermoelastic contraction modeling: Tectonophysics, v. 400, p. 179–207, https://doi.org/10.1016/j.tecto.2005.03.002.

Prothro, L., 2018, Geologic framework model for the underground nuclear explosions signature experiment P-tunnel testbed, Aqueduct Mesa, Nevada National Security Site: Mission Support and Test Services Report DOE/NV/03624-0312.

Prothro, L., and Warren, R., 2001, Geology in the vicinity of the TYBO and BENHAM underground nuclear tests, Pahute Mesa, Nevada Test Site: Bechtel Nevada Report DOE/NV/11718-305.

Prothro, L.B., Drellack, S.L., and Mercadante, J.M., 2009, A hydrostratigraphic system for modeling groundwater flow and radionuclide migration at the corrective action unit scale, Nevada Test Site and surrounding areas, Clark, Lincoln, and Nye Counties, Nevada: National Security Technologies Report DOE/NV/25946-630.

Repstock, A., Heuer, F., Im, J., Hubner, M., Schulz, B., Breitkreuz, C., Gilbricht, S., Fischer, F., and Lapp, M., 2019, A late Paleozoic Snake River-type ignimbrite (Planitz vitrophyre) in the Chemnitz Basin, Germany: Textural and compositional evidence for complex magma evolution in an intraplate setting: Journal of Volcanology and Geothermal Research, v. 369, p. 35–49, https://doi.org/10.1016/j.jvolgeores.2018.11.010.

Riley, P.R., Goodwin, L.B., and Lewis, C.J., 2010, Controls on fault damage zone width, structure, and symmetry in the Bandelier Tuff, New Mexico: Journal of Structural Geology, v. 32, p. 766–780, https://doi.org/10.1016/j.jsg.2010.05.005.

Ross, C.S., and Smith, R.L., 1961, Ash-flow tuffs: Their origin, geologic relations, and identification: U.S. Geological Survey Professional Paper 366, 81 p.

Sammis, C.G., 1991, A damage mechanics source model for underground nuclear explosions: PL-TR-91-2103: Phillips Laboratory Air Force Systems command Hanscom Air Force Base, 21 p.

Sammis, C.G., 2004, Generation of high frequency P and S wave energy by rock fracture during a buried explosion: Its effect on P/S discriminants at low magnitudes: AFRL-VS-HA-TR-2004-1208: Air Force Research Laboratory, 23 p.

Sawyer, D.A., Fleck, R.J., Lanphere, M.A., Warren, R.G., Broxton, D.E., and Hudson, M.R., 1994, Episodic caldera volcanism in the Miocene southwestern Nevada volcanic field: Revised stratigraphic framework, $^{40}Ar/^{39}Ar$ geochronology, and implications for magmatism and extension: Geological Society of America Bulletin, v. 106, p. 1304–1318, https://doi.org/10.1130/0016-7606(1994)106<1304:ECVITM>2.3.CO;2.

Short, N.M., 1966, Effects of shock pressures from a nuclear explosion on mechanical and optical properties of granodiorite: Journal of Geophysical Research, v. 71, no. 4, p. 1195–1215, https://doi.org/10.1029/JZ071i004p01195.

Short, N.M., 1968, Nuclear-explosion-induced microdeformation of rocks: An aid to the recognition of meteorite impact structures, *in* French, B.M., and Short, N.M., eds., Shock Metamorphism of Natural Materials: Baltimore, Maryland, Mono Book Corp., p. 185–210.

Skurtveit, E., Torabi, A., Gabrielsen, R.H., and Zoback, M.D., 2013, Experimental investigation of deformation mechanisms during shear-enhanced compaction in poorly lithified sandstone and sand: Journal of Geophysical Research: Solid Earth, v. 118, p. 4083–4100, https://doi.org/10.1002/jgrb.50342.

Slate, J.L., Berry, M.E., Rowley, P.D., Fridrich, C.J., Morgan, K.S., Workman, J.B., Young, O.D., Dison, G.L., Williams, V.S., McKee, E.H., Ponce, D.A., Hildenbrand, T.G., Swadley, W.C., Lundstrom, S.C., Ekren, E.B., Warren, R.G., Cole, J.C., Fleck, R.J., Lanphere, M.A., Sawyer, D.A., Minor, S.A., Grunwald, D.J., Laczniak, R.J., Menges, C.M., Yount, J.C., and Jayko, A.S., 1999, Digital geologic map of the Nevada Test Site and vicinity, Nye, Lincoln and Clark Counties, Nevada and Inyo County, California: U.S. Geological Survey Open-File Report 99–554A, scale: 1:120,000, 54 p. text, https://doi.org/10.3133/ofr99554A.

Soden, A.M., Lunn, R.J., and Shipton, Z.K., 2016, Impact of mechanical heterogeneity on joint density in a welded ignimbrite: Journal of Structural Geology, v. 89, p. 118–129, https://doi.org/10.1016/j.jsg.2016.05.010.

Sun, Y., and Carrigan, C.R., 2014, Modeling noble gas transport and detection for the comprehensive nuclear-test-ban treaty: Pure and Applied Geophysics, v. 171, no. 3–5, p. 735–750, https://doi.org/10.1007/s00024-012-0514-4.

Swanson, E.M., Sussman, A.J., Wilson, J.E., Townsend, M.J., Prothro, L.B., and Gang, H.E., 2018, Multi-scale fracture damage associated with underground chemical explosions: Journal of Structural Geology, v. 110, p. 142–154, https://doi.org/10.1016/j.jsg.2018.02.008.

Swanson, E.M., Sussman, A.J., and Wilson, J.E., 2019, Rapid clay precipitation in explosion-induced fractures: Geology, v. 47, p. 1176–1180, https://doi.org/10.1130/G46957.1.

Sweetkind, D.S., and Drake, R.M., II, 2007, Characteristics of fault zone in volcanic rocks near Yucca Flat, Nevada Test Site, Nevada: U.S. Geological Survey Open-File Report 2007-1293, 52 p., https://doi.org/10.2172/920108.

Terhune, R.W., 1971, Prediction of underground nuclear explosion effects in Wagon Wheel Sandstone, nuclear explosions—peaceful applications: Livermore, California, Lawrence Radiation Laboratory, University of California, TID-4500, UC-35, UCRL-50993, Rev. 1.

Underwood, E., 1970, Quantitative Stereology: Reading, Massachusetts, Addison-Wesley Publishing Company, 274 p.

U.S. Department of Energy, 2015, United States Nuclear Tests July 1945 through September 1992, National Nuclear Security Administration Nevada Field Office, Las Vegas, NV: DOE/NV-209-REV 16.

Wagner, K., Prothro, L., and Larotonda, J., 2018, Drilling, completion, and geology of core hole UE-12p#7, Aqueduct Mesa, Nevada National Security Site: Mission Support and Test Services Report.

Wilmarth, V.R., 1959, Structural changes, *in* Diment et al., ed., Geologic Effects of the Rainier Underground Nuclear Explosion: U.S. Geological Survey Trace Elements Investigations Report 355.

Wilson, J.E., Chester, J.S., and Chester, F.M., 2003a, Microfracture analysis of fault growth and wear processes, Punchbowl fault, San Andreas system, California: Journal of Structural Geology, v. 25, p. 1855–1873, https://doi.org/10.1016/S0191-8141(03)00036-1.

Wilson, J.E., Goodwin, L.B., and Lewis, C.J., 2003b, Deformation bands in nonwelded ignimbrites: Petrophysical controls on fault-zone deformation and evidence of preferential fluid flow: Geology, v. 31, no. 10, p. 837–840, https://doi.org/10.1130/G19667R.1.

Zwiessler, R., Kenkmann, T., Poelchau, M.H., Nau, S., and Hess, S., 2017, On the use of a split Hopkinson pressure bar in structural geology: High strain rate deformation of Seeberger sandstone and Carrara marble under uniaxial compression: Journal of Structural Geology, v. 97, p. 225–236, https://doi.org/10.1016/j.jsg.2017.03.007.

Science Editor: Wenjiao Xiao
Associate Editor: Pengfei Li

Manuscript Received 20 January 2022
Revised Manuscript Received 25 April 2022
Manuscript Accepted 12 July 2022

Printed in the USA